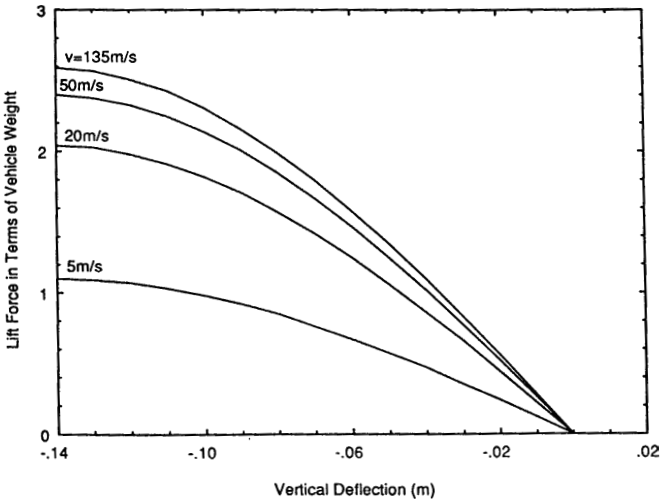

Figure 68. Lift force vs. vertical deflection (Foster-Miller).

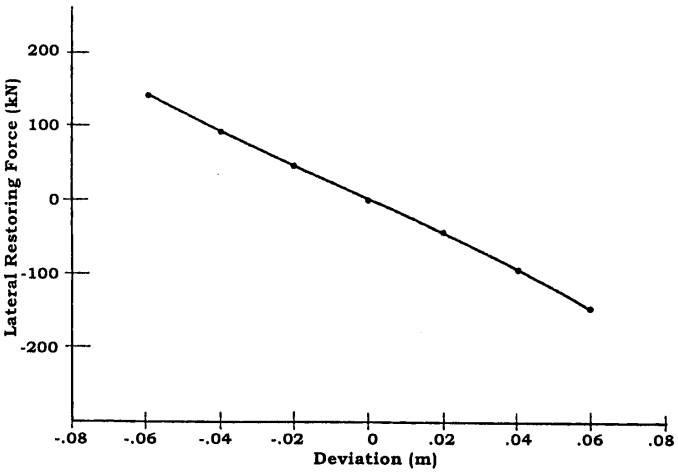

a. Foster-Miller's calculations.

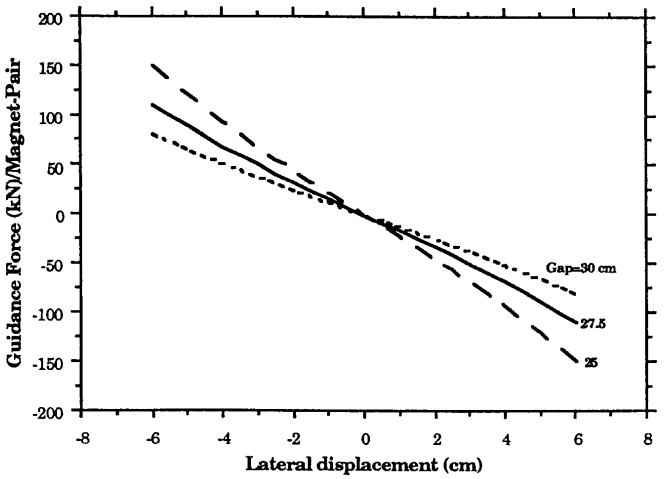

b. Our calculations for various air gaps.

Figure 69. Guidance force vs. lateral deflection.

marginal lift will be reduced. Normal takeoff and landing will presumably occur in tangent sections of the track and should not require the full safety margins provided for high-speed operation.

Since the coils in this system can be wound with multiple turns, the conductors can be thinner than the skin depth. Thus, increases in resistivity induced by skin effects are not a concern. The calculations assume copper conductors in the guideway with the cross-sectional area indicated.

The primary guidance forces in this system result from interaction of the vehicle magnets with the cross-connected propulsion coils. Foster-Miller's calculated guidance forces for one pair of magnets as functions of lateral displacements of the vehicle are shown in Figure 69a. Our calculation of the corresponding force is shown in Figure 69b and is lower by about 15%. The total restoring force for a 0.030-m lateral displacement is calculated to be about 400 kN. Smaller, additional guidance forces result from the propulsion current in the coils and from interactions with the null-flux coils that provide levitation.

Modeling results for stray fields. Magnets on opposite sides of the vehicle have been arranged to have the same polarity in this design, resulting in lower magnetic fields at the center of the cabin than would occur if the magnets had opposite polarities. Foster-Miller's calculation of the field at floor level is shown in Figure 70a and confirmed by our calculation shown in Figure 70b. Although this polarization scheme reduces the field in the center of the cabin, the field at the side of the cabin is little affected by the polarization, as can be seen by comparing Figure 70b and Figure 71.

The fields in a vertical plane near the windows and extending along the length of the vehicle were calculated for the latter case and are shown in Figure 72. In this figure, the passengers closest to the magnets would be located at the 10.5-m position. The fields in the cross section centered over the bogie array (the 6-m point of Fig. 72) are shown in Figure 73. (The view is from the front of the vehicle; no seats are located in this plane.) Referring to Figure 72, we can see that the field at this symmetrical position between the magnets is actually lower than in other planes along the axis of the vehicle. A five-sided ferromagnetic

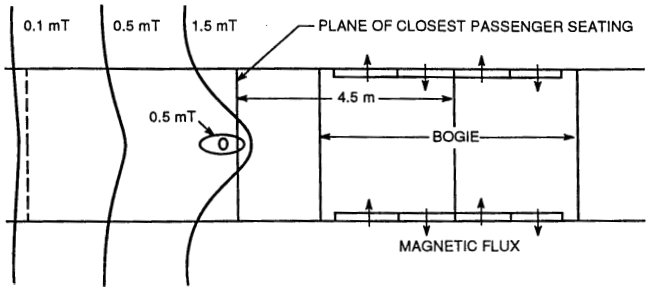

a. Foster-Miller's calculations.

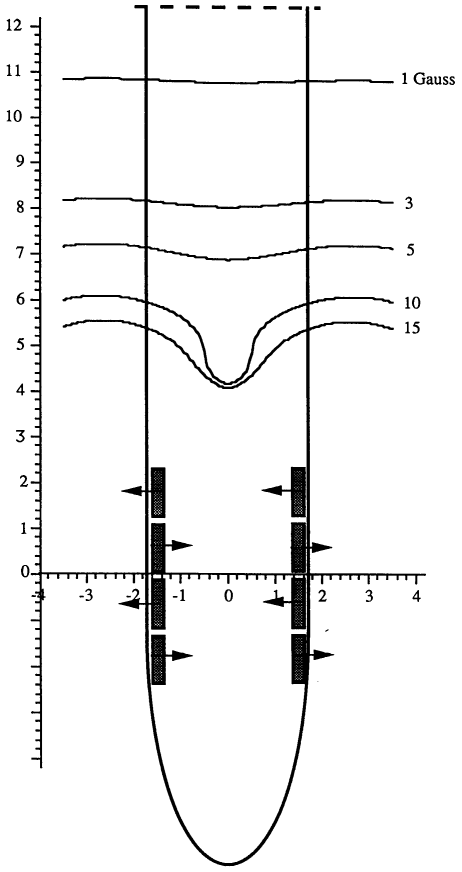

b. Our calculations (floor level, no bucking coils).

Figure 70. Top view of stray fields for Foster-Miller aiding-flux arrangement.

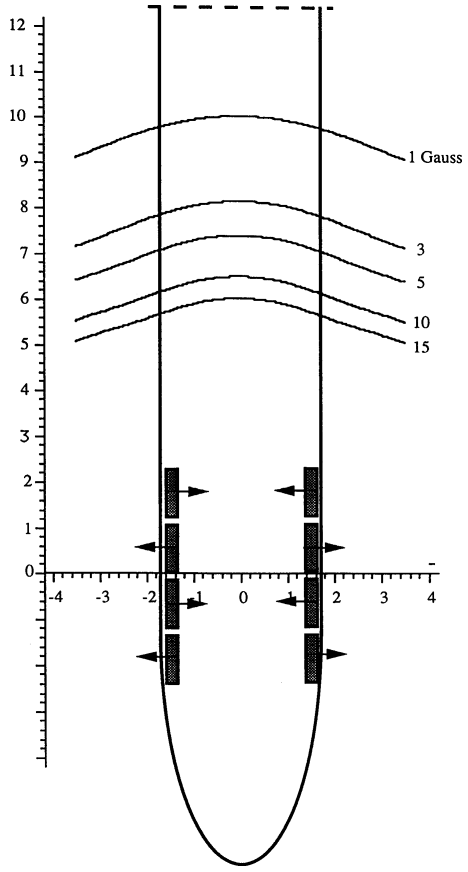

Figure 71. Top view of stray fields for Foster-Miller canceling-flux arrangement (floor level, no bucking coils).

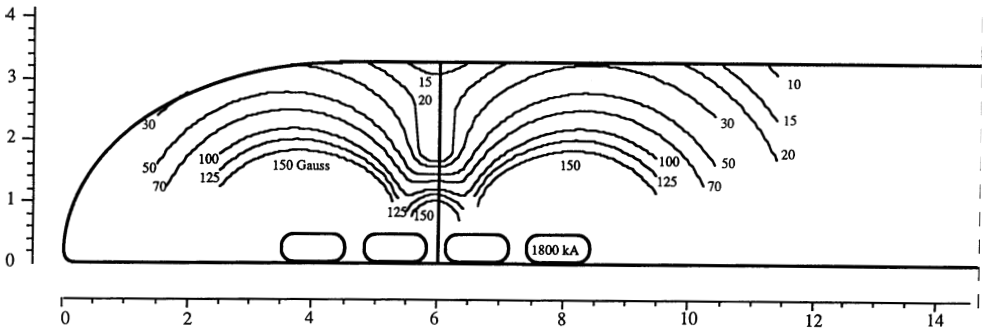

Figure 72. Side view of stray fields for Foster-Miller vehicle near a window.

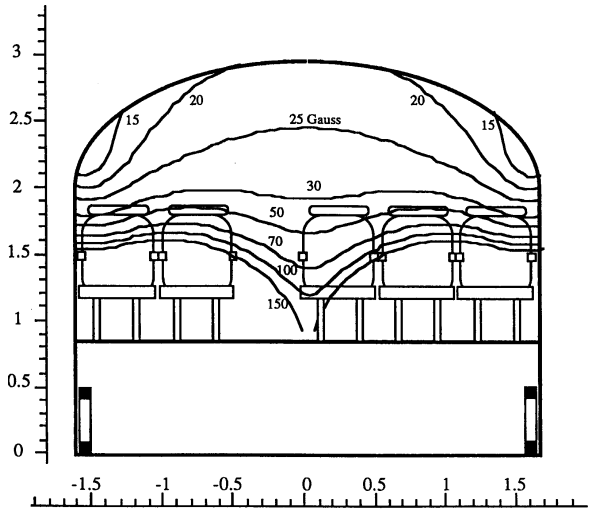

Figure 73. Cross-sectional view of stray fields for Foster-Miller's vehicle at center of magnet array (6-m point of Fig. 72).

shield around the passenger compartment is proposed to lower the fields in this compartment further. Although the fields of Figures 72 and 73 have not been extended outside the vehicle, the external fields near the magnets will clearly be rather intense and will not be significantly reduced by the use of the ferromagnetic shield.

Grumman

Unique features. The Grumman conceptual design (see Fig. 5) is an EMS system using constant-current superconducting magnets to generate the magnetomotive force for the iron poles of the onboard magnets. The magnetic field is dynamically controlled by separate trim coils near the pole faces of the magnet. In addition, the gap between the iron poles and the LSM stator is increased from the 8–10 mm used in TR07 to 40 mm. Unlike the TR07 system, which uses separate magnets for suspension and guidance, this system uses one set of magnets acting against a single reaction plate (the stator of the LSM) that is mounted at a 35° angle from horizontal in the guideway. This concept, unlike TR07, requires that a restoring force be generated when the magnets are displaced sideways on the rail. The baseline vehicle carries 100 passengers and weighs 61.4 tonnes.

Model used for analysis. We used the three-dimensional finite-element code TOSCA to analyze this system because of our concerns about the effects of fringing of the field in the long gap of this system.

Modeling results. The baseline magnetic structure is shown in Figure 74. The pole faces are square with sides of 0.200 m and react against a square cross-section rail also having sides of 0.200 m. Inside the superconducting magnet, the iron core is 0.280 m in diameter (Fig. 74a). The corresponding motor pole pitch is 0.75 m. The superconducting magnet has an inside diameter of 0.330 m and an outside diameter of 0.380 m

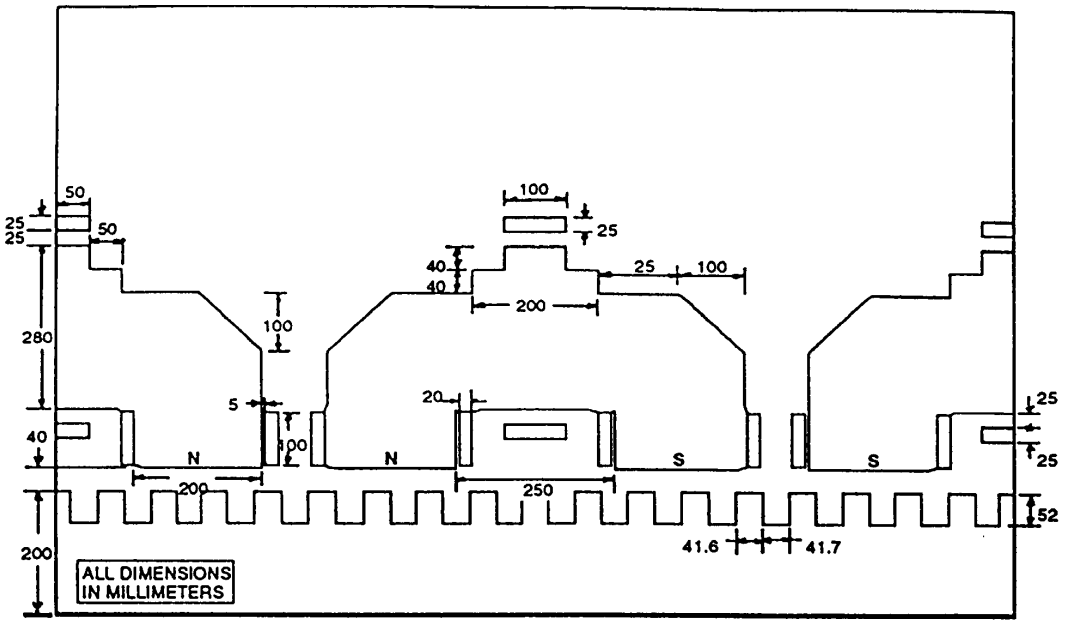

a. Pole and rail geometry.

Figure 74. Baseline magnetic structure of the Grumman concept.

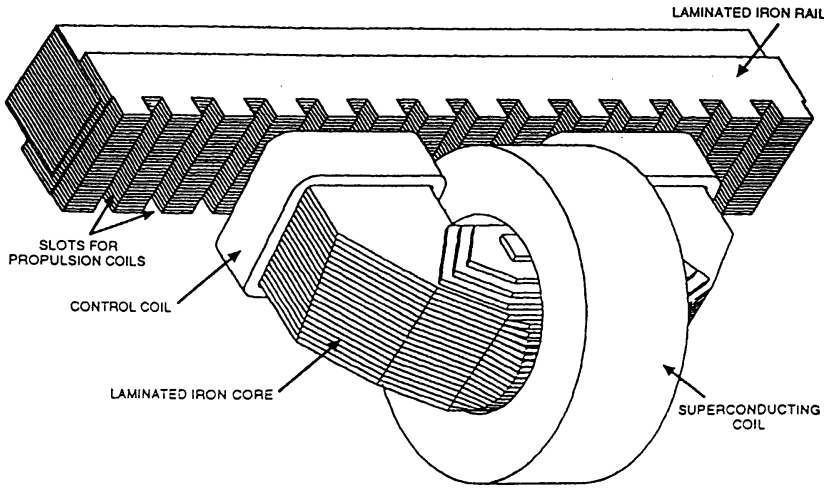

b. Electromagnetic suspension system.

Figure 74 (cont'd). Baseline magnetic structure of the Grumman concept.

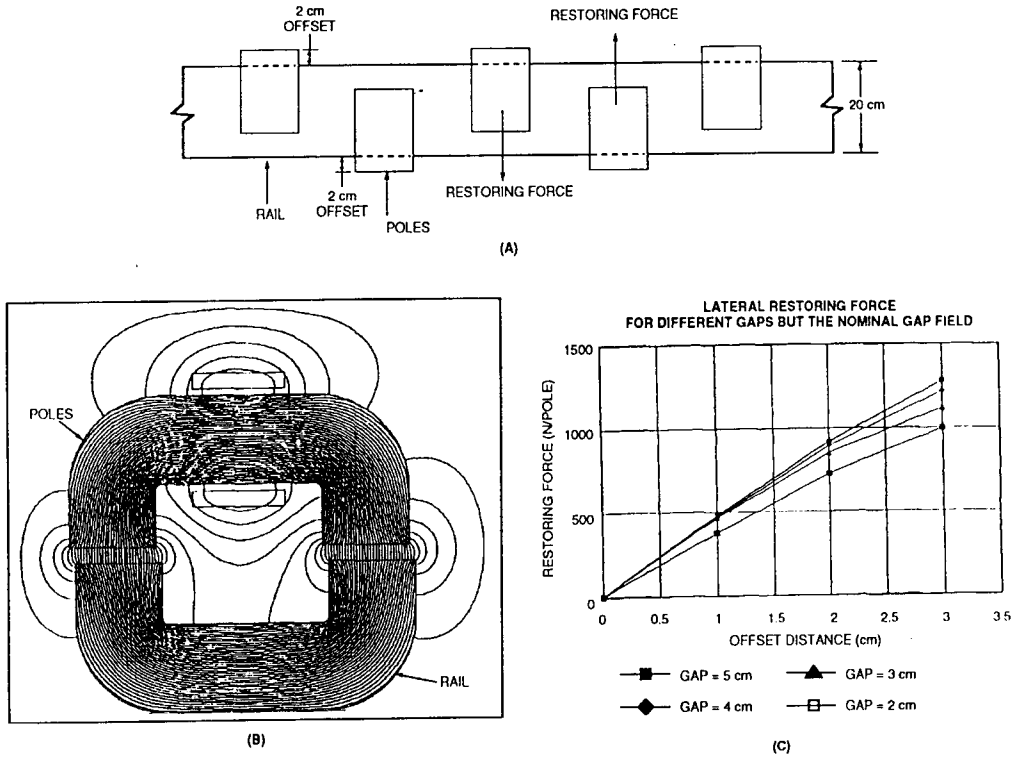

Figure 75. Pole arrangement and resulting lateral forces (Grumman).

(Fig. 74a). These dimensions are inconsistent with the "coil diameter" of 0.288 m given in the final report and the dimensions of the iron pole. This inconsistency has more effect on the mechanical structure than the magnetics. It is possible that the legs of the "C" magnet might have to be lengthened to accommodate the cryostat, which has an extremely limited capacity of helium above the magnet. Grumman has chosen to use 48 magnets of this type, 24 on each side of the vehicle. The arrangement of the magnets on the rail provides stability as the magnet moves to the side of the rail (Fig. 75). Each pole extends to the side of the rail by 0.020 m. A typical matrix of points on which the fields were calculated is shown in Figure 76.

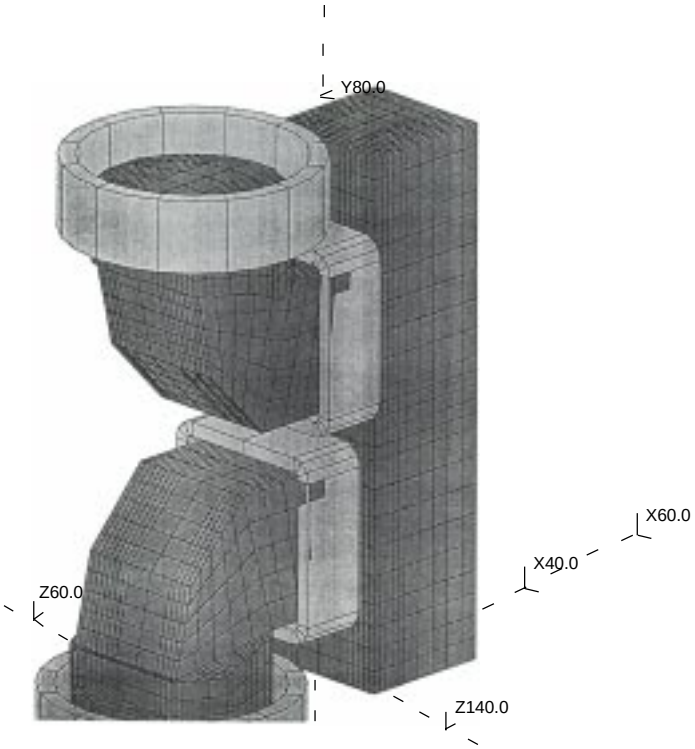

Figure 76. Typical matrix array for finite-element analysis of Grumman suspension.

The baseline configurations used in the calculations are given in Table 35.

Model results for levitation and guidance. The Grumman vehicle magnets interact with a single reaction rail (i.e., stator pack) on each side of the vehicle to generate levitation, guidance, and propulsion forces. This approach inherently couples levitation and guidance forces. We calculated the magnetic forces in the directions perpendicular to and parallel to the reaction-rail face for comparison with Grumman's computed results. These are the fundamental suspension forces. The actual vertical and horizontal guidance forces are combinations of these values, and their control is the major issue addressed in section 3.2.4.

Table 35. Baseline configuration used in Grumman's analysis and our TOSCA analysis.

Parameter	*Units*	*Grumman*	*Tosca*
Pole pitch	m	0.75	0.75
Number of poles	—	48	48
Pole–rail gap	m	0.040	0.040
Iron-core diameter	m	0.28	0.28
Pole dimensions	m	0.20×0.20	0.20×0.20
Pole material	—	Vanadium-Permendur	M43
Rail width	m	0.20	0.20
Rail thickness	m	0.20	0.20
Rail material	—	M43	M43
Current per pole	kA	50	50

The calculated forces normal to the faces of the poles (referred to as both the normal force and the total lift force) are shown in Figure 77 as functions of the current in the trim coils with the baseline current of 50 kAT in the superconducting magnet. The trim coil current in the Grumman figure (Fig. 77b) is shown as that in a single trim coil, while ours is the sum of the currents in both trim coils, accounting for the factor of two difference in these currents. A more detailed comparison of the agreement between the two computations is shown in Figure 78. The vertical lift force on the vehicle is the sum of these normal forces on each magnet, multiplied by cos35°. At the nominal operating point shown, the vertical force is about 940 kN, while the vehicle weighs about 630 kN, so a provision of 50% in lift has been made for cornering, wind, and safety factors.

The suspension controller can feed different control currents to magnets on opposite sides of the vehicle. This generates a lateral guidance force equal to the difference between forces on opposing sides, multiplied by sin35°. This requires no verification because the forces derive from the total lift force verified above (see Fig. 78).

The suspension also generates restoring forces for motion parallel to the face of each rail. The configuration of the magnets that provides this stabilization force was shown in Figure 75. In this configuration, alternate magnets are located 0.020 m beyond their respective sides of the rail. There is no net restoring force in this position. As the magnets are displaced, one moves onto and the other off of the rail, resulting in a force that tends to restore the magnets to their equilibrium positions. Grumman calculated the restoring force shown in Figure 75 for the case where the magnetic field in the gap is constant. The capability of specifying a constant gap field is not contained in TOSCA, so we varied the current to approximate this condition, and then scaled the forces to the appropriate fields using a field-strength squared (B^2) scaling to obtain the results shown in Figure 79. This approach approximates a condition in which the normal force is constant.

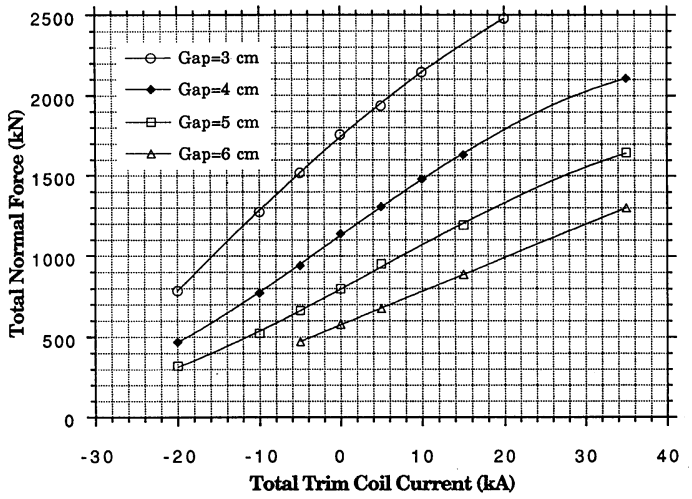

a. Our calculations with total current in the trim coils as variable, assuming a constant 50-kAT current in the superconducting magnets.

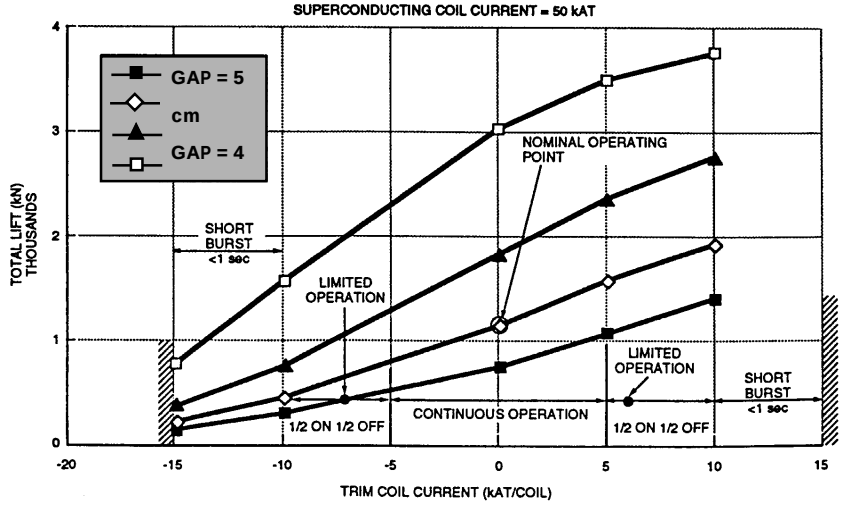

b. Grumman's calculations with current in a single trim coil as variable, assuming a constant 50-kAT current in the superconducting magnets.

Figure 77. Total normal force vs. trim current for Grumman suspension.

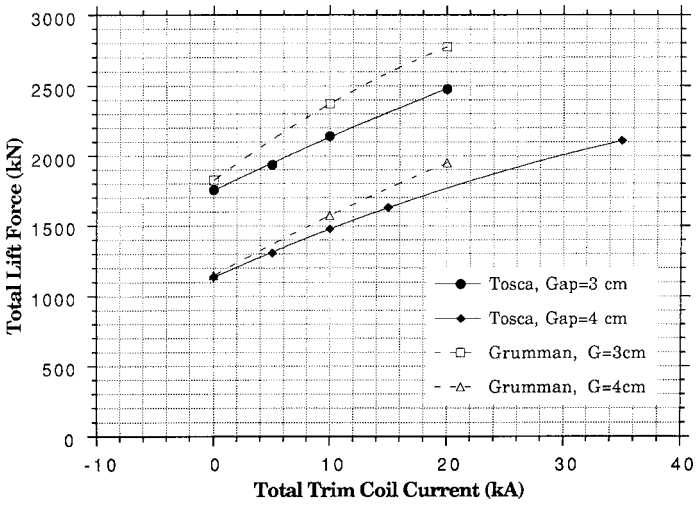

Figure 78. Comparison between ANL and Grumman computations of lift forces (with trim coil as variable; Isc *= 50 kA).*

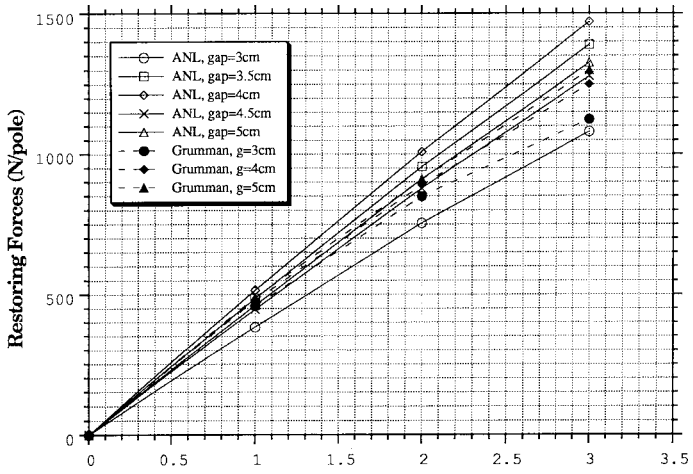

Figure 79. Comparison between ANL and Grumman computations of restoring forces for one magnet moved parallel to rail face (gap field = 0.75 T*).*

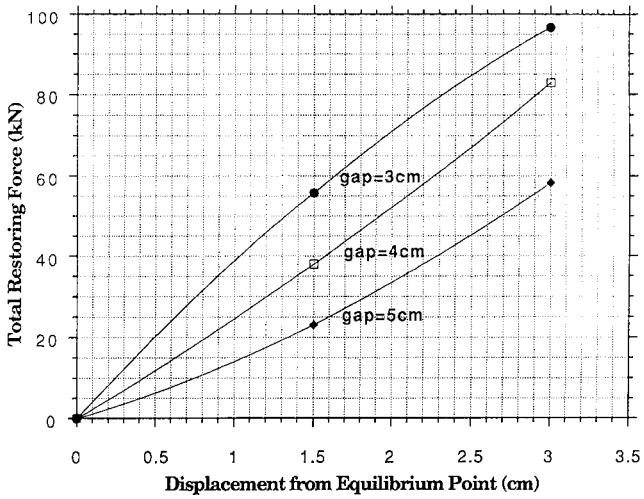

*Figure 80. Grumman restoring force for constant current for one magnet moved parallel to rail face (*I *= 50 kA).*

The restoring force is stabilizing with all the gap spacings evaluated, with our results indicating a somewhat greater variation with the gap dimension than do the Grumman data.

If the current rather than the field is maintained constant, the results of Figure 80 are obtained, telling us that the restoring force increases as the gap decreases.

Modeling results for stray fields. The magnetic fields in both the TR06 / TR07 and the Grumman system are better confined than in any of the EDS systems using superconducting magnets. The field in the cabin is more uniformly distributed along the length of the vehicle since the magnets are in a row beneath it. The magnetic fields around the magnets are shown in Figure 81. The fields external to the vehicle will be of the same magnitude.

Magneplane

Unique features. The Magneplane system (see Fig. 6) is the only continuous sheet levitation system proposed by the SCD contractors. In this setup, eight magnets aboard the vehicle induce currents in aluminum sheets in the guideway as the vehicle passes over. These currents in turn interact with the magnets to produce repulsive forces between the vehicle and the guideway. The guideway, shaped as a trough, permits the vehicle to roll in a turn, avoiding the use of a separate tilt mechanism. Continuous-sheet guideways, unlike those using discrete coils, provide a smoother interaction with the supercon-

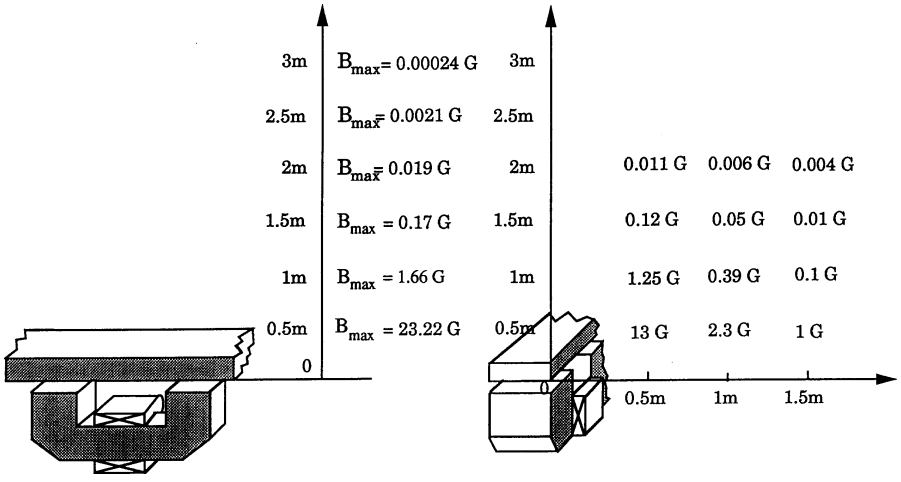

*Figure 81. Stray fields around the center of Grumman magnet (*I *= 50 kA;* g *= 4 cm).*

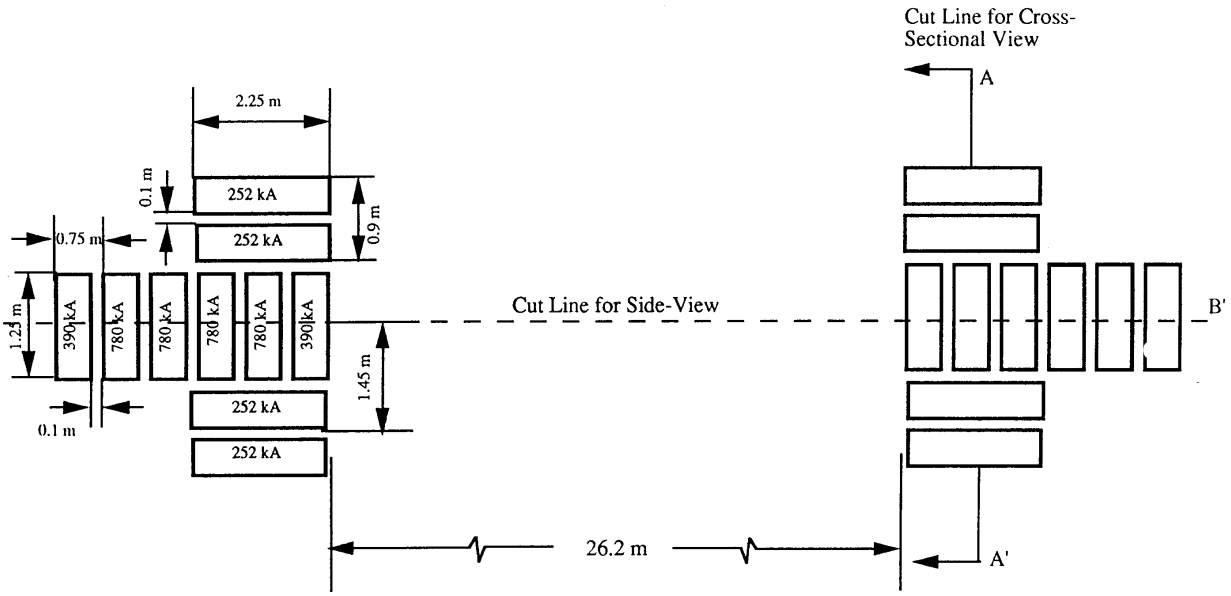

Figure 82. Layout of Magneplane's superconducting coils (A–A' in Fig. 89a).

ducting magnets, simplifying the achievement of ride comfort, and reducing the AC losses in the cryostat and magnet. The system is stabilized in the roll direction by the interaction of the propulsion coils with the edge of the guideway and by airfoils. Propulsion of the system is analogous to the other EDS systems, except that the 12 magnets used are separate from those used for levitation, and the LSM windings are under the vehicle. The dimensions, currents, and layout of the magnets are shown in Figure 82.

Model used for analysis. The stray fields for the Magneplane system were analyzed in the same manner as those in the other systems.

Analytical models are available for calculating the magnetic lift and drag forces on magnets moving above an infinitely wide conducting ground plane. Analyses for single magnets have been given by Chilton and Coffey (1971), Coffey et al. (1972), Coffee et al. (1973), Reitz (1970), and Davis and Reitz (1972). A similar analysis has been made by Lee and Menendez (1974) for multiple magnets. The latter formulation was programmed and used in the analysis of this system. Values for a single magnet obtained using this formulation compare well with a previous program based on the above-mentioned references, which has been validated at ANL by numerous experiments. The guideway is sufficiently wide that the results are expected to be affected only marginally by its finite width.

Electrodynamic interactions of magnets with the edges of finite conductors as encountered in the keel stabilization of the magplane have not been solved in analytical form and require computer computation using finite-element analyses. The ELEKTRA computer code discussed earlier is capable, in principle, of performing this task. In practice, however, the problem could only be addressed in reduced sizes at very low velocities that are insufficient for evaluating the details of this interaction.

Modeling results for levitation and guidance. The lift and drag forces were calculated for two levitation magnets shown in the previous figure and configured for the baseline 45-passenger vehicle. The lift and drag forces for a bogie composed of two sets of two magnets are shown in Figure 83. The variation of the levitation force with the suspension height, with the velocity as a parameter, is shown in Figure 84. This figure shows the effective spring constant of the vehicle. Since the baseline force demanded of this bogie is 76 kN, we found that sufficient force can be generated by the proposed magnets. The vehicle is guided by allowing it to rotate in the trough-shaped guideway so separate guidance magnets are not used.

Modeling results for keel effect. Owing to limitations of the program used and the capabilities of the computers available, the forces resulting from the interaction of the propulsion magnets with the finite width guideway could be calculated only at

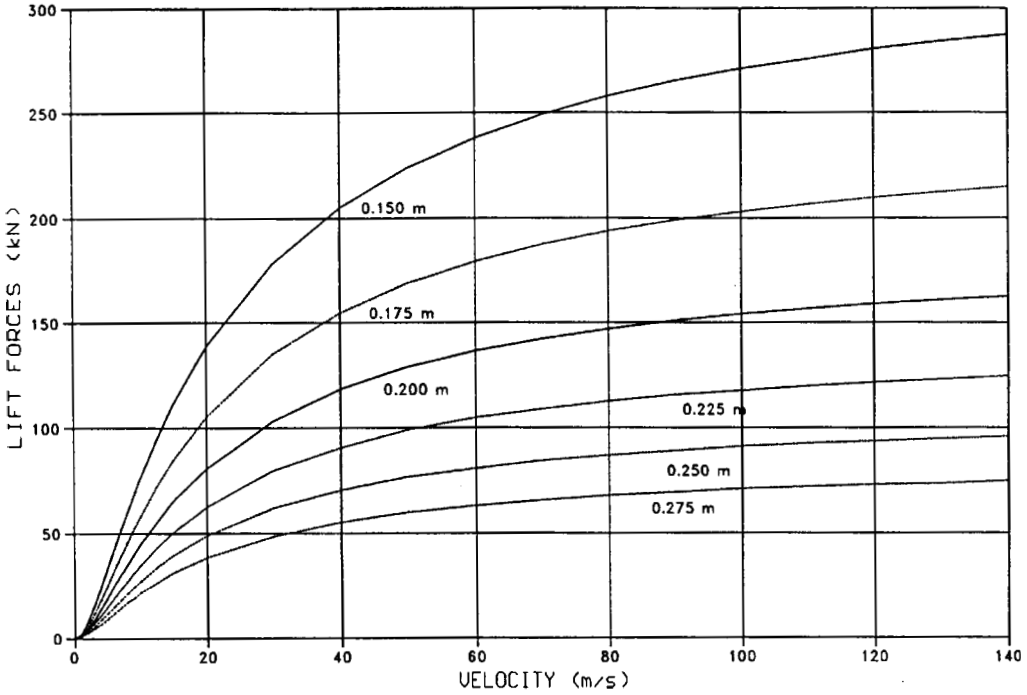

a. Lift forces (2.25 m long, 0.4 m wide, and 0.1 m spacing).

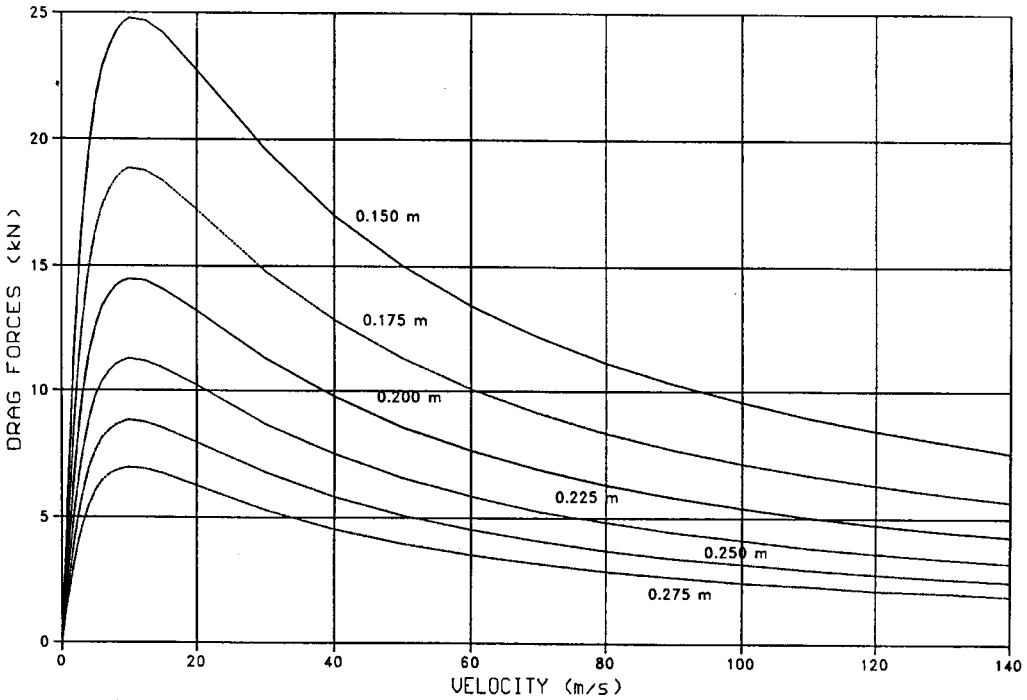

b. Drag forces (2.25 m long, 0.4 m wide, and 0.1 m spacing).

Figure 83. Lift and drag forces for a single bogie of the 45-passenger Magplane (ANL).

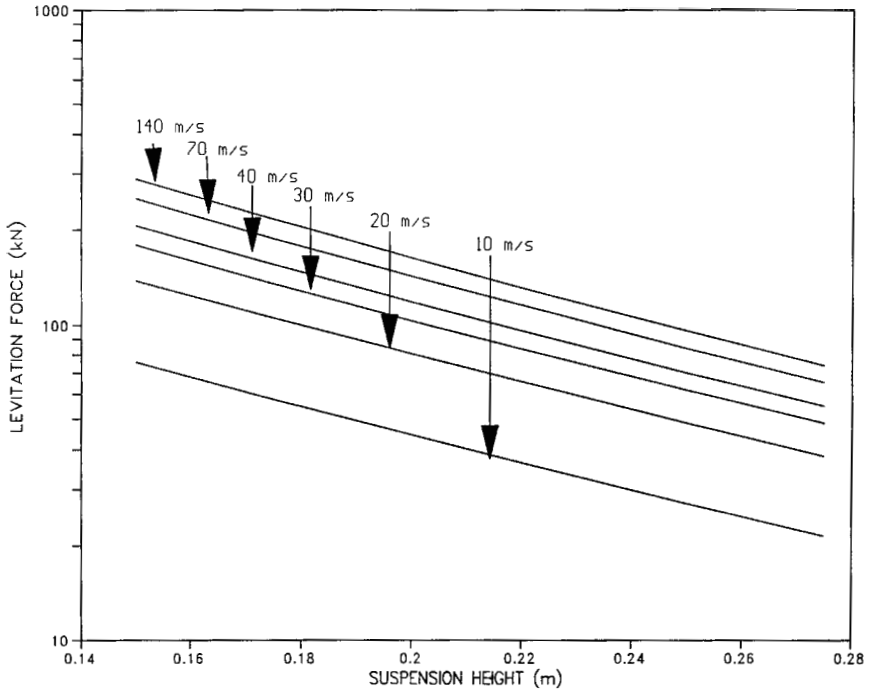

Figure 84. Lift force vs. suspension height for Magplane (ANL).

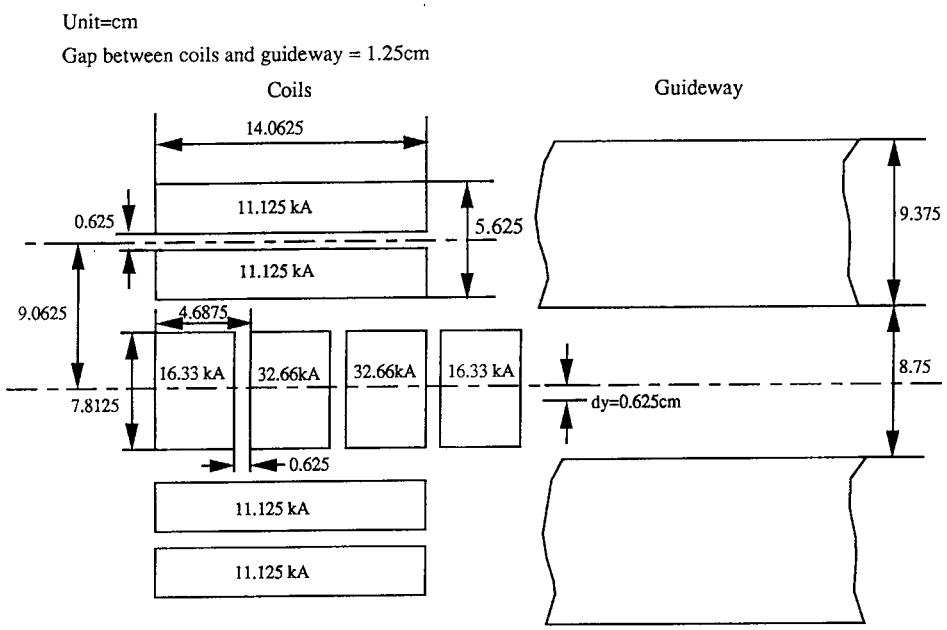

Figure 85. Layout used in Magneplane's analysis for a reduced-size vehicle (ANL).

very low velocities and in greatly reduced sizes. By arbitrarily reducing the size of the vehicle *and the current* by a factor of 16 (see Fig. 85), we obtained the eddy current patterns of Figure 86 at a velocity of 6 m/s. (The Magneplane system uses six propulsion magnets rather than the four modeled here.) In Figure 86a, the eddy current distribution in the guideway induced by the propulsion magnets alone is shown. In Figure 86b, the eddy current induced by the combination of the propulsion and levitation magnets is shown. The forces resulting from these interactions are relied upon to provide roll stabilization of the vehicle. The force tending to restore the vehicle

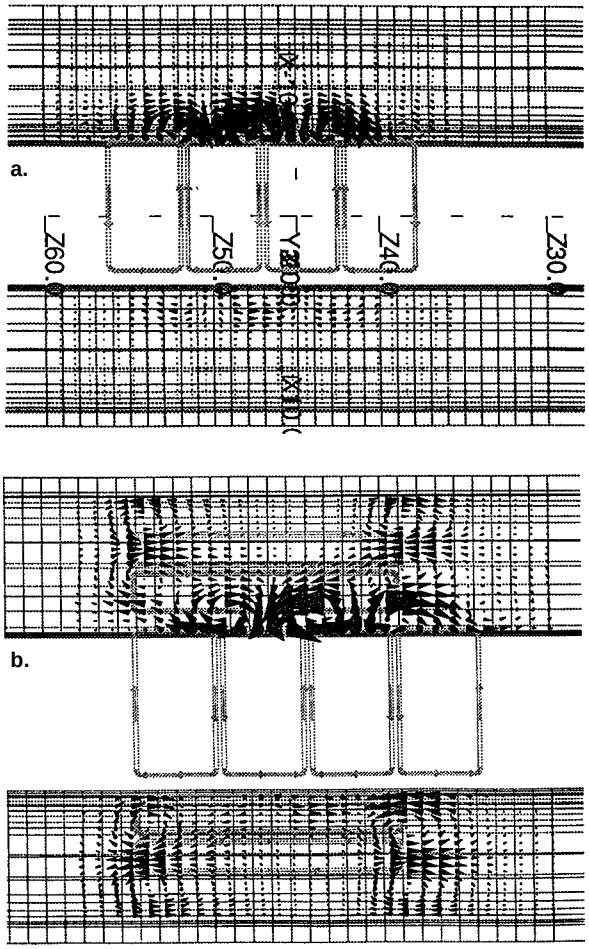

Figure 86. Eddy current patterns from Magneplane's analysis for a reduced-size vehicle (velocity = 6 m/s). The top figure shows the effect of four propulsion magnets alone. The bottom figure shows the eddy currents induced by the four propulsion coils together with the levitation magnets (ANL).

to its neutral position upon displacement laterally by 0.625 cm is shown in Figure 87. We have not attempted to extrapolate this force to a full scale system. That is, although we are able to verify the physical principle of the keel effect, we are unable at present to verify its magnitude.

Modeling results for stray fields. As in the other EDS systems, the most intense stray fields occur when the vehicle is at rest and no currents induced in the guideway oppose the fields generated by the magnets on the vehicle. Our calculated fields along the centerline of the vehicle (Fig. 88a) are comparable to those presented by Magneplane (Fig. 88b). Magneplane proposes to use active normally conducting coils to reduce these fields (Fig. 88c). These cancellation coils were not modeled, but are expected to work as proposed. The computed fields in the cross section A–A′ of Figure 82 (i.e., the centerline of the levitation coils) are shown in Figure 89a, neglecting the effects of the field cancellation coils. The predicted height of the 50-G contour is comparable to that found by Magneplane. Figure 89b shows the fields at this same cross section calculated by Magneplane for the case in which the cancellation coils are active. The active coils substantially reduce field strengths near the vehicle floor. Magneplane did not present a figure for the case where the coils are inactive.

Viability issues. To the extent that the suspension systems have been analyzed in this work, we regard all systems as being capable of generating the forces presented in their respective reports. The analysis of the Magneplane system is more limited than are those for the other systems for the reasons discussed above. No assessment was

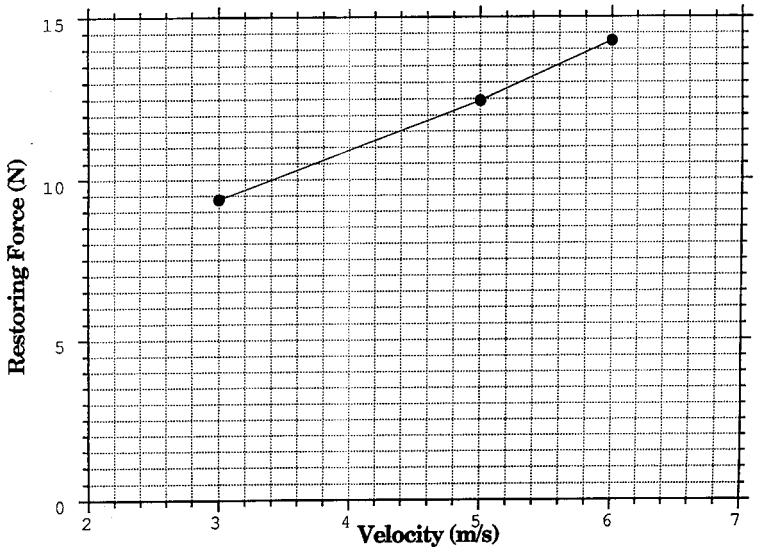

Figure 87. Restoring forces from Magneplane's analysis for a reduced-size vehicle (displacement = 0.625 cm) (ANL).

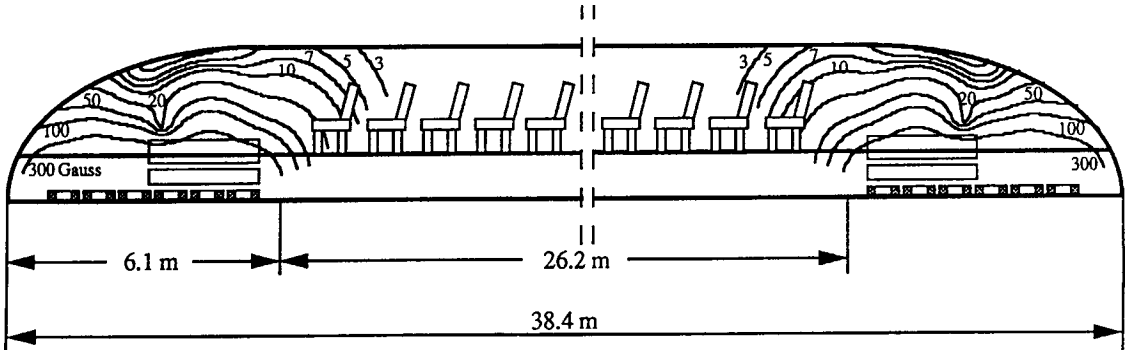

a. Our calculations along the center plane of the vehicle.

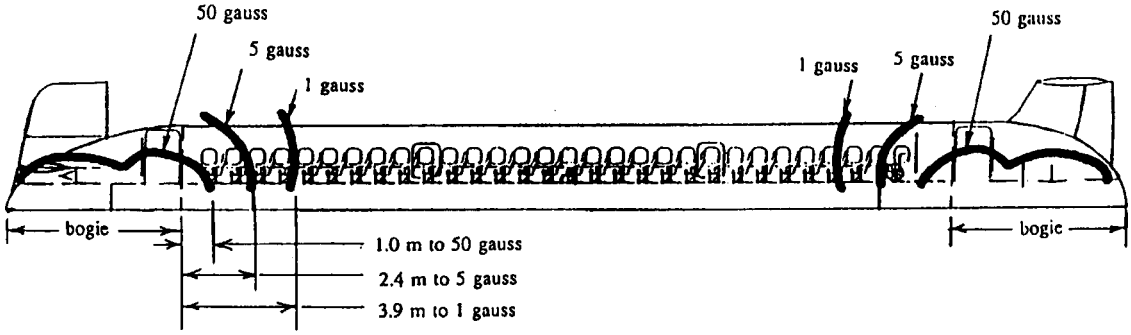

b. Magneplane's calculations in a 140-passenger Magplane with no active shielding coils.

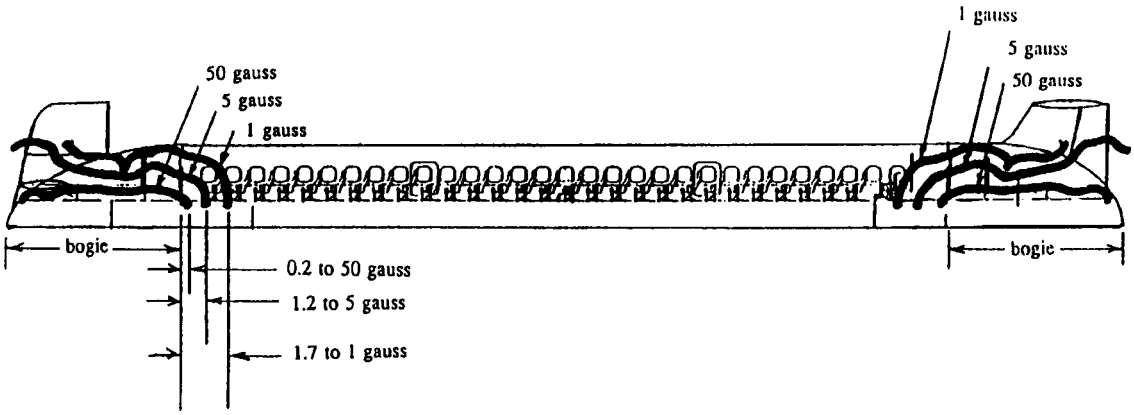

c. Magneplane's calculations in a 140-passenger Magplane with active shielding coils near bogies.

Figure 88. Side view of centerline stray fields in the Magplane.

made of the viability of the superconducting magnets or the cryogenics as they are proposed. A complete assessment will require that these components be evaluated in detail.

In particular, the superconducting magnets and the cryostats containing them will be subjected to eddy current heating caused by the time-varying fields resulting from interaction of the magnets with the guideway. The time variation is caused by the ordinary dynamic motions of the vehicle during operation, by guideway roughness, and by the discontinuous nature of the coils in some of the guideways. Although these interactions were not analyzed, they could require that the magnets be designed with greater margins of safety than proposed by the contractors.

The use of Nb_3Sn magnets in a conduit is an innovative approach. More information and

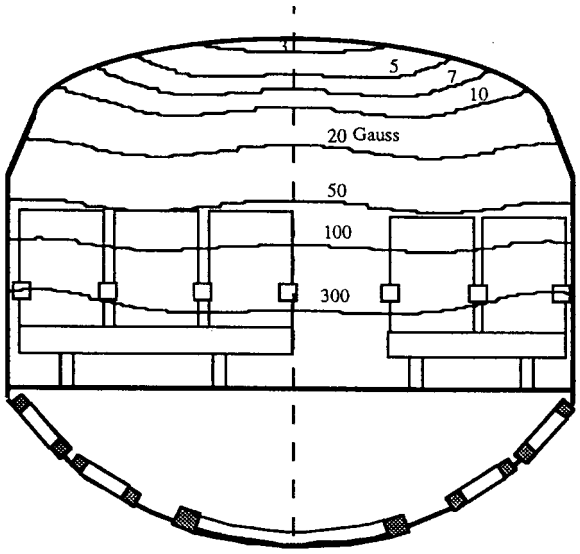

a. Our calculations of those in plane A–A′ of Figure 82.

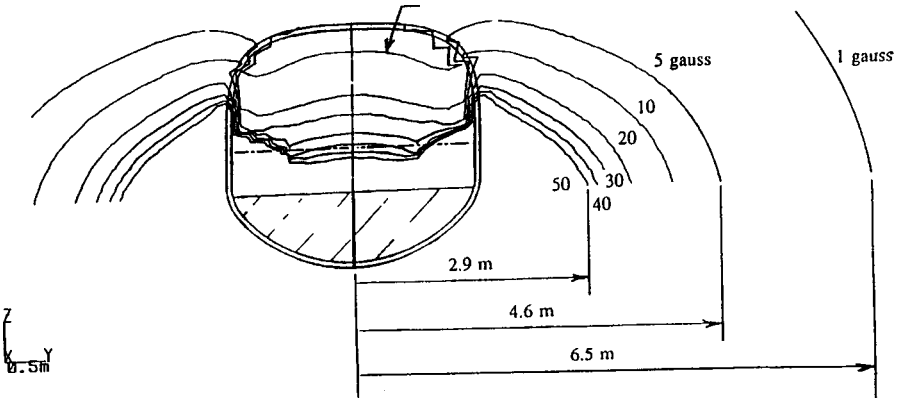

b. Magneplane's calculations of those in plane over a bogie.

Figure 89. Cross-sectional view of stray fields.

experimental data on the performance of these magnets in this application will be required before such systems are deployed. Since adjacent magnets are coupled magnetically, the quench of one magnet will result in a rapid change in current in neighboring magnets and a change in the distribution of the vehicle's load on the guideway. This effect was not evaluated.

The ultimate viability of the various systems is determined by the use of these magnet systems in conjunction with other systems and controls to safely levitate and guide the proposed vehicles. These considerations entail the analysis of the dynamic performance of the vehicle with the guideway, as discussed in the next section.

No attempts were made to optimize the systems proposed by the contractors, and further improvements in the systems proposed might or might not be possible.

3.2.4 Vehicle–guideway interaction*

Objectives

The primary functions of a maglev vehicle suspension are to follow the guideway and to isolate passengers from local guideway variations. These functions translate, respectively, into safety and ride-comfort requirements. The suspension must meet these requirements without imposing excessive forces on the guideway and without needing excessive stroke. These requirements influence selection of guideway stiffness, guideway strength, geometric tolerances, suspension actuators, and controls, and these choices in turn affect guideway and vehicle costs.

* Written by David Tyrell, U.S. Department of Transportation.

This section summarizes the GMSA's assessment of the dynamic vehicle–guideway interactions of TR07 and the four SCD concepts. Our objectives were to determine the advantageous features of each suspension, the features of each that might lead to problems, and the areas warranting further effort. Owing to available time and resources, these analyses focused solely on the vertical dynamics of each concept.

Methodology

The approach used for this effort has been to review each concept, evaluate its performance capability, and do a detailed study of potentially critical performance limitations. The analyses varied for each concept to address specific concerns identified during preliminary assessments. For TR07 the major concern is a magnet striking the guideway because of its small gap. For the Bechtel concept, the major concern is the implementation of its active suspension, consisting of both active aerodynamic surfaces and active elements between the magnet bogies and the vehicle body. For the Foster-Miller concept, the major concern is ride quality owing to its use of discrete bogies and a passive secondary suspension. For the Grumman concept, the major concern is the force–range capability of its levitation control magnets. And for the Magneplane concept, the major concern is the physical implementation of its proposed semi-active suspension.

Traditionally, ground-based vehicles have used a primary suspension with a relatively high natural frequency (5 to 10 Hz) and low damping (0 to 5% of critical damping) to follow the guideway closely, and a secondary suspension with a relatively low natural frequency (0.8 to 1.4 Hz) and relatively high damping (30 to 50% of critical damping) to isolate the passengers. This traditional terminology remains helpful in classifying suspensions, whether they possess passive or active elements or indeed combine the functions of separate primary and secondary suspensions into a single suspension.

Variations in guideway geometry result from its design and construction, the service loads imparted by the vehicle, the environment (soil movement, thermal cycling, snow and ice build-up, etc.), and maintenance. We may describe these geometric variations as the sum of random variations and discrete events. Random variations result from such things as nonuniformity of materials, and discrete events result from design characteristics such as column spacing.

To represent vertical random geometry of a rigid guideway, we used a power spectral density (psd) of the form

$$G(\omega) = \frac{AV}{\omega^2} \tag{1}$$

where $G(\omega)$ = psd of the guideway ($m^2/[rad/s]$)
A = amplitude factor (equal to 6.1×10^{-8} m for high-quality welded rail)
V = speed of vehicle (m/s)
ω = frequency of interest (rad/s).

The discrete perturbations modeled here are those attributable to guideway precamber and flexibility. We modeled the guideway as a simply supported beam, either single span or double span, as shown in Figure 90. We calculated dynamic deflection of the guideway for the flexible-guideway analyses.

We consider the guideway geometry to be the sum total of the random roughness, the precamber, the guideway flexibility, and any irregularities owing to environmental influences. We have not modeled the latter here. How well the vehicle behaves on the rigid and flexible guideways indicates the margin that is allowable for the irregularities owing to environmental influences.

A general difficulty with our modeling is the choice of A (psd amplitude factor) in the absence of measurements for maglev concepts. As a

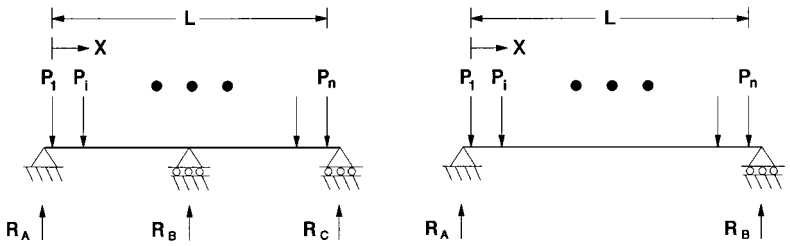

a. Double-span guideway beam. *b. Single-span guideway beam.*

Figure 90. Guideway dynamic model.

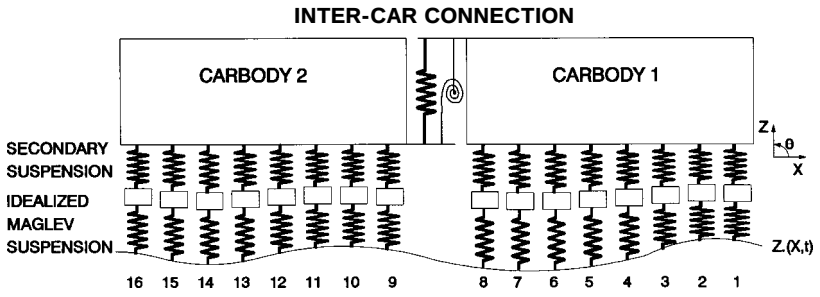

Figure 91. TR07 vertical dynamics model.

baseline, we selected the value measured for U.S. Class 6 railroad track ($A = 6.1\times10^{-8}$ m). This is quite high-quality track suitable for 110-mph (49-m/s) passenger rail operation. Our dynamic analysis of TR07 suggests that it was designed for a random guideway roughness near this value. We also examined the maximum amplitude tolerated by each maglev system, based on ride comfort or safety considerations, and compared this with our baseline value. Such comparisons reveal the construction-tolerance requirements for the maglev systems relative to those of high-speed rail.

Application to TR07

The major concern for TR07 is a magnet striking the guideway, owing to what appears to be a small nominal gap of 8 mm. Gap variations may be caused by the guideway flexibility and by variations in the guideway geometry. The TR07 guideway is generally elevated, and as the vehicle traverses the suspended guideway, the guideway deflects. The suspension of the vehicle responds to this guideway deflection, and to guideway geometry variations such as random roughness, precamber, and misalignment between beams. Either excessive guideway flexibility or geometry may cause poor ride quality and potentially may cause a magnet to strike the guideway.

The vertical dynamics model of TR07 is shown in Figure 91. The model used for the flexible guideway analysis is a two-span guideway. The parameters of the model are listed in Table 36. Although TR07 uses active control of its levitation- and guidance-magnet currents, we may analyze it as a passive primary suspension with fixed natural frequency and damping. We discuss the procedure for determining the equivalent passive suspension for TR07 in the section dealing with Grumman's active suspension.

Figure 92 shows, for speeds of 100, 300, and 500 km/hr (28, 83, and 139 m/s), vehicle response over a rigid guideway corresponding to high quality welded rail construction ($A = 6.1\times10^{-8}$ m).

Plotted in Figure 92 are the RMS accelerations at the front of the lead section of the vehicle. Note that, at 500 km/hr, the 10-Hz, one-third-octave band response is 0.024 g RMS, whereas the ISO 1-hour reduced comfort boundary at 10 Hz is 0.048 g RMS. If the only irregularity was random roughness (i.e., a rigid guideway), a guideway with a roughness coefficient of $A = 12.2\times10^{-8}$ m could be tolerated, based on ride comfort.

Table 36. TR07 model parameters.

Description	*Value*
Vehicle	
Inertia	
Hinge mass	1016 kg
Carbody mass	45,711 kg
Carbody pitch inertia	2.48×10^6 kg m^2
Stiffness	
Primary stiffness	1.45×10^6 N/m
Secondary stiffness	2.26×10^5 N/m
Intercar vertical stiffness	2.26×10^7 N/m
Intercar pitch stiffness	0 N m
Damping	
Primary damping	3.45×10^4 N s/m
Secondary damping	2.15×10^4 N s/m
Intercar vertical damping	0 N s/m
Intercar pitch damping	0 N m s
Geometry	
Distance between magnets	3.125 m
Guideway	
Material	
Modulus of elasticity	21.0×10^9 N/m^2
Density	2.41×10^3 kg/m^3
Geometry	
Cross-section area	1.508 m^2
Area moment of inertia	0.682 m^4
Damping	
First mode	3%
Second mode	3%

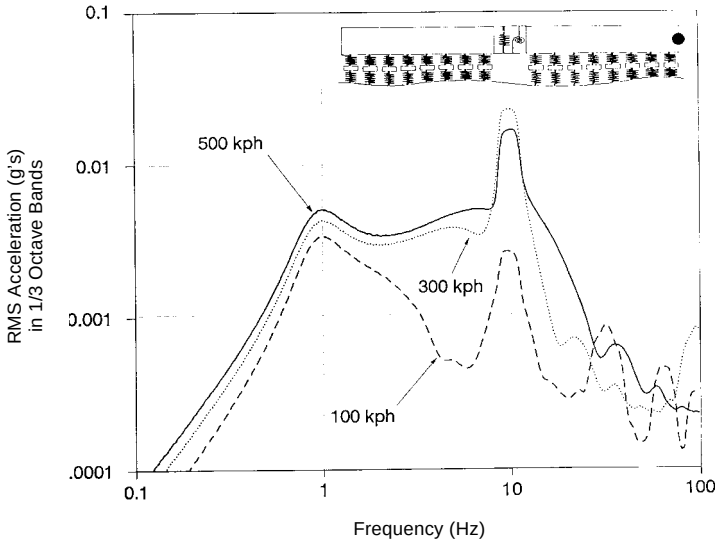

Figure 92. TR07 RMS acceleration vs. frequency (front of vehicle, random roughness).

The corresponding RMS gap variation at 500 km / hr is 1.05 mm. If we assume that 3σ represents the maximum excursion likely, the magnet gap must be at least 3.2 mm. For TR07's 8-mm gap, the maximum permissible roughness coefficient for a rigid guideway would be $A = 15.3\times10^{-8}$ m. This is a less severe requirement than that for ride comfort. Consequently, ride quality dictates the maximum random vertical guideway geometry variations that TR07 can tolerate.

The vehicle response is influenced by guideway flexibility. As the guideway becomes more flexible, gap variations and carbody accelerations tend to increase in magnitude. Figure 93 shows graphs of gap variation and ride quality as functions of guideway flexibility, both for constant and varying beam natural frequencies. The graph has been constructed such that thresholds for both the gap variations and ride quality coincide. Figure 93 indicates that both gap variation and ride quality thresholds are reached for essentially the same guideway flexibility, and that these thresholds are reached for less flexibility if the guideway's natural frequencies are allowed to vary. The graphs also show that, even if a larger magnet gap existed, guideway flexibility would still need to be sufficiently small to provide acceptable ride quality.

For a TR07-type of vehicle, ride quality dictates the flexibility of the guideway. Guideway flexibility in turn dictates the range of the magnet gap variation that must be accommodated. For this type of vehicle, a maglev suspension that could accommodate an increased range of gap variations would *not* allow an increase in guideway flexibility, owing to the requirement of acceptable ride quality. The consequences of poor ride quality may include nausea and fatigue of the occupants; however, these consequences tend to be short-lived. The consequences of one or more magnets exceeding its allowable gap variation and potentially striking the guideway may be long-lived and costly.

TR07 would benefit in two ways from having a larger magnet gap. First, it would increase its safety margin; second, it would allow the vehicle to maintain acceptable ride quality over a rougher guideway. To realize the second benefit, however, TR07 would need either an active secondary suspension or more control authority in its active primary suspension. Such improvements would require substantial redesign of TR07's existing suspension.

Application to SCD concepts

Bechtel. Our major concern for the Bechtel concept is the achievement of an active suspension consisting of both active aerodynamic surfaces and active elements between the magnet bogies and the vehicle body. Active suspension control can potentially allow acceptable ride quality over rougher, more flexible guideways than is possible with passive suspensions. Bechtel's final report did not describe the control strategy for its active suspension or the hardware anticipated for its actuators and controllers. Without such informa-

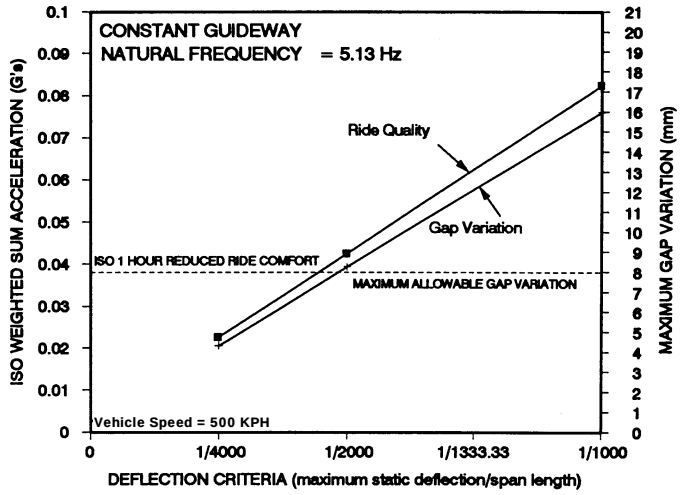

a. Constant guideway.

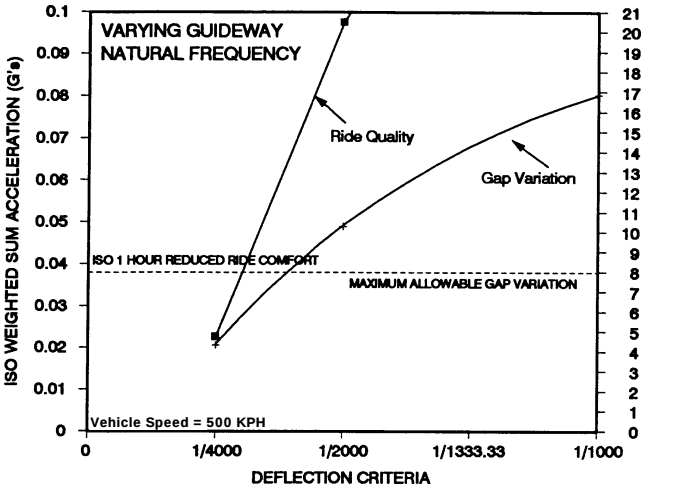

b. Varying guideway.

Figure 93. Influence of guideway flexibility on TR07 gap variations and ride quality.

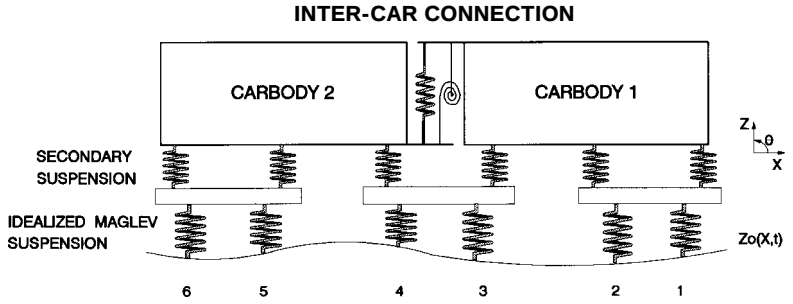

Figure 94. Foster-Miller vehicle model.

tion, the vehicle–guideway interaction of Bechtel's concept cannot be analyzed.

Foster-Miller. Our major concern for the Foster-Miller design is ride quality, and the guideway geometry necessary to provide it. The Foster-Miller vehicle is supported by articulated intermediate bogies between the cars, and by end bogies supporting the ends of the first and last cars. The vehicle model is shown in Figure 94, and the parameters of the model are listed in Table 37. For the flexible guideway analysis, the Foster-Miller guideway is modeled as a double-span beam.

The vertical secondary suspension is lightly damped (about 6%), compared with about 30% for most rail passenger vehicles and about 50% for

most highway passenger vehicles. This light damping, in combination with the vehicle being supported by widely spaced bogies rather than by distributed bogies (like those used on TR07, the Grumman design, and the Bechtel design), tends to make the vehicle response to the flexible guideway sensitive to vehicle speed.

Figure 95 shows the vehicle response to the flexible guideway with a 3-mm precamber. With 6% damping, vertical acceleration at the front of the vehicle exceeds 0.08 g's at 480 km/hr (133 m/s). Increasing the secondary suspension damping to 36% decreases this acceleration to 0.045 g's.

The precamber of the guideway is 3 mm. However, the maximum deflection of the guideway at low speeds is 1 mm and is 1.8 mm at 500 km/hr. Reducing the precamber to approximately one-half the low speed deflection of the guideway would also reduce the maximum carbody accelerations.

Table 37. Foster-Miller model parameters.

Description	*Value*
Vehicle	
Inertia	
Bogie mass	7,380 kg
End bogie mass	6,130 kg
"A" vehicle mass	22,630 kg
Carbody pitch inertia	2.48×10^6 kg m^2
Stiffness	
Primary stiffness	2.651×10^6 N/m
Secondary stiffness	
End bogie	1.2×10^6 N/m
Intermediate bogie	0.6×10^6 N/m
Intercar vertical stiffness	0 N/m
Intercar pitch stiffness	0 N m
Damping	
Primary damping	0 N s/m
Secondary damping	1.0×10^4 N s/m
Intercar vertical damping	0 N s/m
Intercar pitch damping	0 N m s
Geometry	
Distance between magnets	varies (m)
Guideway	
Material	
Modulus of elasticity	30.0×10^9 N/m^2
Density	2.40×10^3 kg/m^3
Geometry	
Cross-section area	3.1 m^2
Area moment of inertia	2.16 m^4
Damping	
First mode	0%
Second mode	8%

The acceleration response at the front of the Foster-Miller vehicle to random guideway surface roughness is shown in Figure 96. This figure also shows the response for increased secondary suspension damping. The guideway roughness characteristic used for this analysis is the same as the characteristic used for the analysis of TR07, the results of which are shown in Figure 92. With increased damping, the response of the Foster-Miller vehicle to the random roughness is similar to the TR07 response, indicating that the Foster-Miller vehicle would require similar tolerances on the guideway geometry as TR07.

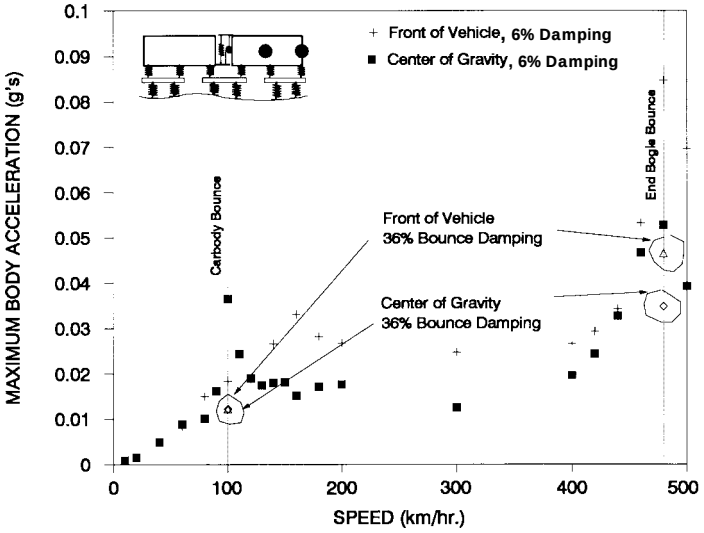

Figure 95. Foster-Miller maximum carbody acceleration vs. speed. Center of gravity and front of vehicle vertical acceleration on a flexible guideway.

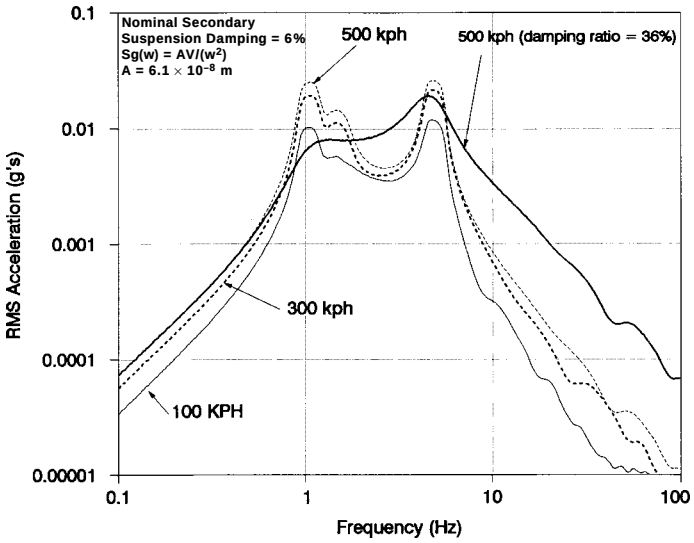

Figure 96. Foster-Miller RMS acceleration vs. frequency (front of vehicle, random roughness, rigid guideway).

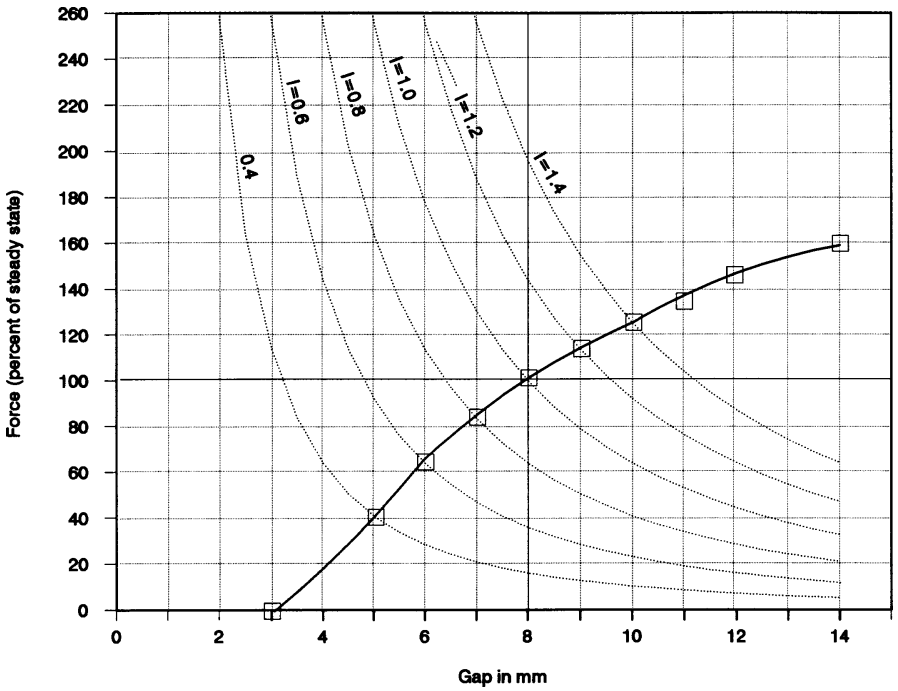

Figure 97. Force–gap characteristics for a typical EMS suspension.

Increasing damping and reducing of guideway precamber are relatively easy to do. We conclude that Foster-Miller's vehicle–guideway interactions would be within allowable ride-comfort and safety limits, provided its random guideway roughness is similar to TR07's. This will require reasonably close tolerances on its null-flux and propulsion coils, but it appears to be achievable.

Grumman. Our major concern with the Grumman vehicle design is the force-range capability of the suspension. The suspension travel must be adequate for the range of guideway perturbations that the vehicle may encounter.

For EMS suspensions, the forces to support the vehicle and to cause it to follow the route alignment are developed by electromagnets interacting with a ferrous reaction rail. This interaction results in a force that attracts the electromagnet to the reaction rail. To maintain the stability of the system, a controller varies the current in the electromagnet's coils as a function of the gap between the electromagnet and the reaction rail and other measurements of the electromagnet's position and velocity. Figure 97 shows the force generated by a typical levitation electromagnet designed to operate at a nominal gap of 8 mm.

The dashed lines in Figure 97 show the force–gap relation that would exist if the current in the electromagnets were kept constant. In this situation, a decrease in gap would result in an increase in the attractive force that would accelerate the electromagnet into the reaction rail, causing an impact. An increase in gap would similarly cause a decrease in the force developed and the force would no longer be large enough to support the weight. Because of this behavior, a permanent magnet or constant current magnet providing levitation by forces of attraction is said to be unstable.

To produce stable levitation forces, the current in the electromagnet is varied as a function of the gap. As the gap becomes smaller, the current is reduced, reducing the attractive force. The electromagnet is then driven away from the reaction rail by the force exerted by the weight of the vehicle. As the gap becomes larger, the current in the electromagnet is increased, resulting in an increase in force produced by the electromagnet, which acts to return it to the nominal gap.

The solid curve in Figure 97 shows the force as a function of gap that would result from a control strategy where the current was changed by 20% of the nominal current for each millimeter of gap change. This force–gap characteristic is believed to represent the electromagnets used in the Transrapid TR06 system and the initial magnets used in the TR07 system.

In Grumman's concept, the force used to support the weight of the vehicle is generated by superconducting coils. These superconducting coils maintain the attraction levitation force with-

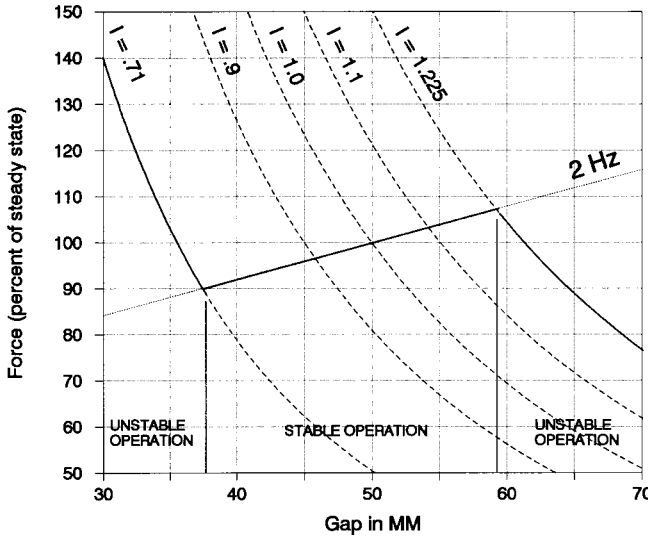

Figure 98. Force–gap characteristics for an electromagnetically trimmed superconducting magnet.

out expending energy in the heating losses associated with an electromagnet. Also, the larger fields generated by the superconducting coils permit the vehicle to maintain a larger equilibrium gap. Stability is established by a set of auxiliary electromagnet coils that adjust the attraction forces by variations in current. The expectation in this approach is that variations in gap and vehicle forces will be small and that a limited electromagnetic field variation will be adequate to maintain control.

Interestingly, the Grumman vehicle does not employ a traditional combination of primary and secondary suspensions. Instead, it uses a single active suspension to follow the guideway closely and to isolate passengers from guideway irregularities.

Figure 98 shows the force–gap characteristic that would be expected for an electromagnetically trimmed superconducting coil magnet that is designed to operate at a gap of 50 mm, with a trim capability to vary the force at the nominal gap 50% either way. The characteristic shown assumes that the control law will maintain an effective stiffness that is equivalent to that of a 2-Hz primary suspension to accommodate dynamic loads. Although Grumman revised their suspension to operate at a gap of 40 mm, the basic conclusions presented here remain valid.

As shown in Figure 98, Grumman's suspension would be stable in a region of gaps between 38 and 59 mm (i.e., a range of 21 mm). This would result in a requirement to keep guideway irregularities at frequencies higher than 2 Hz (or a wavelength of 67 m or less at a speed of 134 m / s) to an amplitude of less than 21 mm peak to peak. Decreasing the system's natural frequency would at most increase the range of stable gaps to 31 mm peak to peak. Increasing the bandwidth of the suspension system has the effect of reducing the range of gap variation that can be tolerated.

Figure 99 shows the block diagram for the force characteristic of a single magnet module of the Grumman maglev vehicle. The guideway's vertical geometry is the vertical position of the guideway at the magnet module, and the vehicle displacement is also at the magnet module. The block diagram shown in the figure is based on the linear-

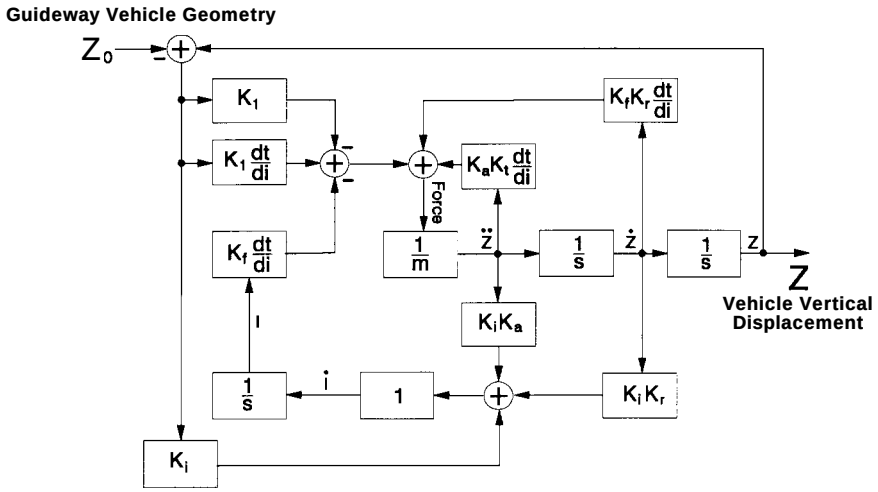

Figure 99. Block diagram of Grumman magnet control system.

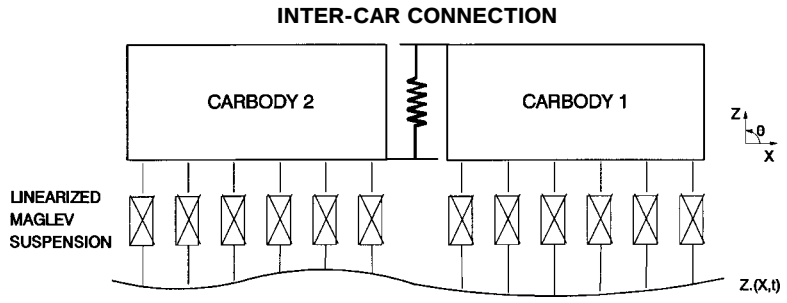

Figure 100. Grumman vehicle model.

ized model developed by Grumman. The model implicitly incorporates the magnet nonlinearities and the magnet module's own servo control.

The force from a magnet acting on the vehicle mass is given by the constant-coefficient differential equation

$$F_n = K_a K_f \frac{\partial f}{\partial i}\ddot{z}_n + K_v K_f \frac{\partial f}{\partial i}\ddot{z}_n + \left(K_f \frac{\partial f}{\partial i} - K_1\right)\left(z_n - zo_n\right) - K_f \frac{\partial f}{\partial i} i_n \qquad (2)$$

where subscript *n* refers to the location of the magnet module. i_n is the current of the particular magnet module, and is given by the constant coefficient differential equation:

$$\dot{i}_n + K_a K_i \ddot{z}_n + K_v K_i \dot{z}_n = K_i\left(z_n - zo_n\right) = 0. \qquad (3)$$

(The force produced by each magnet module is modeled as a point force here, although its behavior is closer to a pressure force. The error from this approximation is small owing to the number of modules supporting each carbody. There are 12 modules with 24 poles supporting each carbody, which were modeled as six forces supporting each carbody.)

The control system diagrammed in Figure 99 and described by eq 2 and 3 is divergently unstable when more than two modules are used to support a single carbody. The carbody motions *Z* and θ are stable, while the magnet module currents i_1, i_2, i_3, i_4, i_5, i_6 are divergently unstable. The following paragraphs discuss the stability of a single carbody supported by six magnet modules controlled using the control loop shown in Figure 99.

Figure 100 shows the model of the baseline Grumman maglev vehicle, which consists of two cars coupled together. Only one carbody of this model is considered in evaluating the stability of a vehicle supported by multiple magnet modules.

There are two equations of motion that describe the behavior of the carbody, and six equations that describe the currents in the magnet modules. These equations are as follows:

$$\left(M + 6K_a K_f \frac{\partial f}{\partial i}\right)\ddot{z} + 6K_v K_f \frac{\partial f}{\partial i}\dot{z} + 6\left(K_f \frac{\partial f}{\partial i} - K_1\right)z - K_f \frac{\partial f}{\partial i}\left(i_1 + i_2 + i_3 + i_4 + i_5 + i_6\right) = \left(K_f \frac{\partial f}{\partial i} - K_1\right)\left(zo_1 + zo_2 + zo_3 + zo_4 + zo_5 + zo_6\right) \qquad (4)$$

$$\left(I + \frac{35}{2}l^2 K_a K_f \frac{\partial f}{\partial i}\right)\ddot{\theta} + \frac{35}{2}l^2 K_v K_f \frac{\partial f}{\partial i}\dot{\theta} + \frac{35}{2}l^2\left(K_f \frac{\partial f}{\partial i} - K_1\right)\theta - lK_f \frac{\partial f}{\partial i}\left(\frac{5}{2}i_1 + \frac{3}{2}i_2 + \frac{1}{2}i_3 - \frac{1}{2}i_4 - \frac{3}{2}i_5 - \frac{5}{2}i_6\right) = l\left(K_f \frac{\partial f}{\partial i} - K_1\right)\left(\frac{5}{2}zo_1 + \frac{3}{2}zo_2 + \frac{1}{2}zo_3 - \frac{1}{2}zo_4 - \frac{3}{2}zo_5 - \frac{5}{2}zo_6\right) \qquad (5)$$

$$\dot{i}_1 + K_a K_i\left(\ddot{z} + \frac{5}{2}l\ddot{\theta}\right) + K_v K_i\left(\dot{z} + \frac{5}{2}l\dot{\theta}\right) + K_i\left(z + \frac{5}{2}l\theta\right) = K_i zo_1 \qquad (6)$$

$$\dot{i}_2 + K_a K_i \left(\ddot{z} + \frac{3}{2} l\ddot{\theta} \right) + K_v K_i \left(\dot{z} + \frac{3}{2} l\dot{\theta} \right) + K_i \left(z + \frac{3}{2} l\theta \right) = K_i zo_2 \quad (7)$$

$$\dot{i}_3 + K_a K_i \left(\ddot{z} + \frac{1}{2} l\ddot{\theta} \right) + K_v K_i \left(\dot{z} + \frac{1}{2} l\dot{\theta} \right) + K_i \left(z + \frac{1}{2} l\theta \right) = K_i zo_3 \quad (8)$$

$$\dot{i}_4 + K_a K_i \left(\ddot{z} - \frac{1}{2} l\ddot{\theta} \right) + K_v K_i \left(\dot{z} - \frac{1}{2} l\dot{\theta} \right) + K_i \left(z - \frac{1}{2} l\theta \right) = K_i zo_4 \quad (9)$$

$$\dot{i}_5 + K_a K_i \left(\ddot{z} - \frac{3}{2} l\ddot{\theta} \right) + K_v K_i \left(\dot{z} - \frac{3}{2} l\dot{\theta} \right) + K_i \left(z - \frac{3}{2} l\theta \right) = K_i zo_5 \quad (10)$$

$$\dot{i}_6 + K_a K_i \left(\ddot{z} - \frac{5}{2} l\ddot{\theta} \right) + K_v K_i \left(\dot{z} - \frac{5}{2} l\dot{\theta} \right) + K_i \left(z - \frac{5}{2} l\theta \right) = K_i zo_6 \quad (11)$$

Table 38 defines and specifies the parameters used in analyses of Grumman's suspension. The displacement, velocity, and current gains depend on the frequency chosen for the magnet module servo control, although this frequency is not directly related to the magnetic force characteristic. We explain below the rationale for examining two equivalent suspension frequencies.

Consider the case when the guideway geometry consists of an even upward displacement of the guideway Z^* and the vehicle and control current have reached steady state, i.e., all their derivatives are 0. Since there is no effective pitch input to the vehicle, the pitch of the vehicle is also 0. These equations then reduce to

$$6\left(K_f \frac{\partial f}{\partial i} - K_1 \right) z - K_f \frac{\partial f}{\partial i} (i_1 + i_2 + i_3 + i_4 + i_5 + i_6) = \left(K_f \frac{\partial f}{\partial i} - K_1 \right) 6Z^* \quad (12)$$

$$lK_f \frac{\partial f}{\partial i} \left(\frac{5}{2} i_1 + \frac{3}{2} i_2 + \frac{1}{2} i_3 - \frac{1}{2} i_4 - \frac{3}{2} i_5 - \frac{5}{2} i_6 \right) = 0 \quad (13)$$

$$K_i z = K_i Z^* . \quad (14)$$

Only two equations contain the six unknown currents, and consequently the currents are divergently unstable. The currents can be made stable in two different ways. One is to add a term in i_n to eq 6–11, which in effect tries to drive the magnet module currents to 0 at all times. This approach involves a substantial revision to the control algorithm. The second approach is to develop a constraint relationship among the currents, such as

Table 38. Grumman vehicle parameters used in analyses.

Description	*Parameter*	*9.1-Hz suspension*	*1-Hz suspension*
Carbody mass	M	30,639 kg	30,639 kg
Carbody pitch inertia	I	8.00×10^5 kg m^2	8.00×10^5 kg m^2
Coupling vertical stiffness	K_{zz}	2.26×10^6 N / m	2.26×10^6 N / m
Distance between magnets	1	2.1 m	2.1 m
Force / gap, open loop	K_1	$4.1\text{x}10^6$ N / m	4.1×10^6 N / m
Force / current	$\partial f / \partial i$	3.33×10^3 N / kAT	$3.33\text{x}10^3$ N / kAT
Current gain	K_i	93 kAT / m s	93 kAT / m s
Magnet servo frequency*	ω_{cl}	60 rad / s	12 rad / s
Acceleration gain	K_a	1.75×10^{-4} s^2	5.75×10^{-4} s^2
Velocity gain	K_v	0.02648 s	0.1517 s
Displacement gain	K_f	1.49×10^4 kAT / m	1.29×10^3 kAT / m

* Affects K_a, K_v, K_f but does not enter directly into analysis.

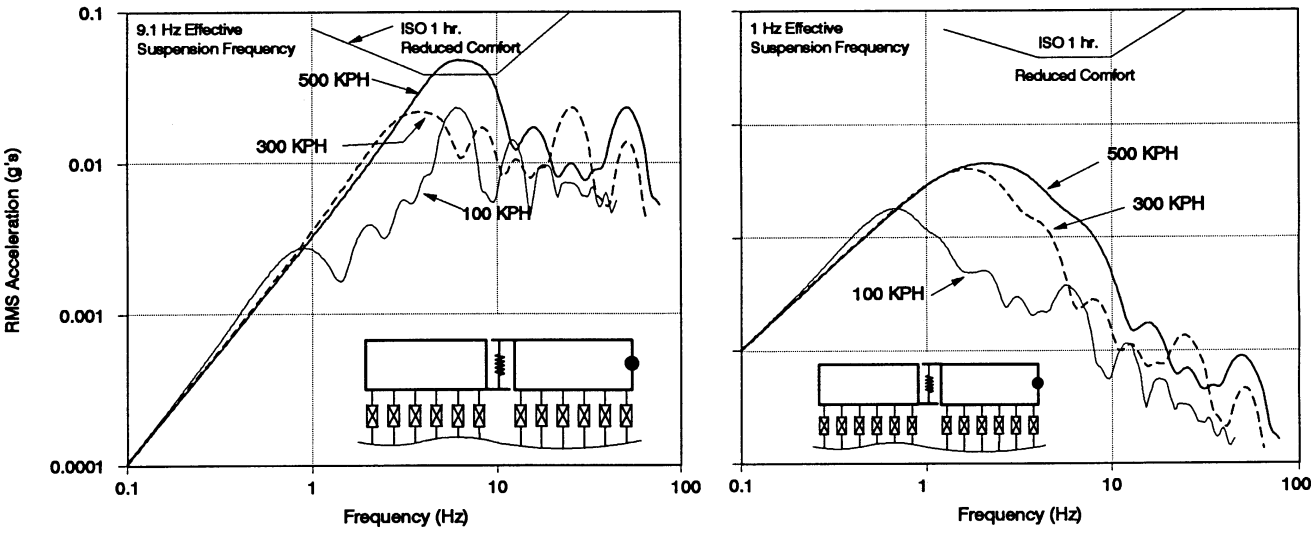

a. 9.1-Hz effective suspension frequency. *b. 1.0-Hz effective suspension frequency.*

Figure 101. Grumman vehicle response to random roughness (rigid guideway).

$i_n = \bar{i} + l_n i'$, where $\bar{i}$ is the average current, l_n is the length from the center of gravity of the car, and i' is the slope required to meet eq 5. This approach does not involve any changes to the control algorithm. However, implementing this approach would involve a substantial change in the philosophy employed in designing the control modules. Grumman's design philosophy requires that the magnet modules be independent of each other as much as possible, while this approach requires the magnet module currents of a carbody to depend upon each other. Nevertheless, we employed this second approach to analyze the Grumman suspension. This makes the force attributable to the currents in the magnet modules behave as analogs to springs. The feasibility of physically implementing this approach has not been evaluated.

The parameter values used by Grumman result in a 9.1-Hz equivalent suspension frequency. Vertically in the steady state, this suspension behaves similarly to a passive suspension with a 9.1-Hz natural frequency and a "skyhook" damping value of 100% (critical damping). Figure 101 shows the response of the model to random roughness in the rigid guideway. As can be seen in the figure, the carbody accelerations exceed the ISO criteria in the front of the vehicle at 500 km / hr.

We wished to determine whether a simple parametric change would allow this suspension to meet the ISO criteria. In the steady state, this suspension can be made to behave similarly to a passive suspension with a 1.0-Hz natural frequency. The carbody accelerations that are calculated for the 1.0-Hz suspension are shown in Figure 101; this suspension easily meets the ISO criteria.

The Grumman guideway is a complex structure. However, the results of the GMSA guideway analysis (section 3.2.1) indicate that the dynamic behavior of the guideway can be approximated as a simply supported beam with a natural frequency of 4.4 Hz and a maximum deflection at the center of the beam of 11 mm when traversed by the baseline vehicle at 500 km / hr. We calculated the response of the vehicle to the flexible guideway. We chose the stiffness such that 11 mm of guideway displacement was calculated at the center of the first guideway beam traversed at 500 km / hr by the vehicle with the 1-Hz suspension, while we chose the mass of the beam such that the first mode frequency of the guideway is 4.4 Hz. The baseline Grumman guideway design has a span length of 27 m and does not call for any precamber of the guideway beams.

Figure 102 shows the maximum carbody accelerations at the center of the vehicle and at the center of gravity of the first car for both the 9.1- and 1-Hz suspensions. The acceleration at the center of the vehicle approaches 1 g for the vehicle with the stiff suspension and reaches 0.12 g for the vehicle with the soft suspension. Although improved by reducing the effective stiffness, the accelerations of the soft suspension are still high relatively high. This is principally ascribable to the

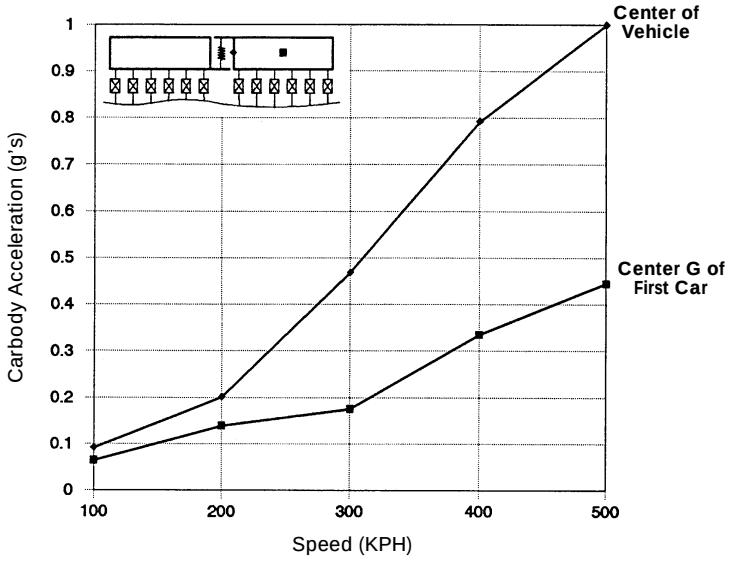

a. 9.1-Hz effective suspension frequency.

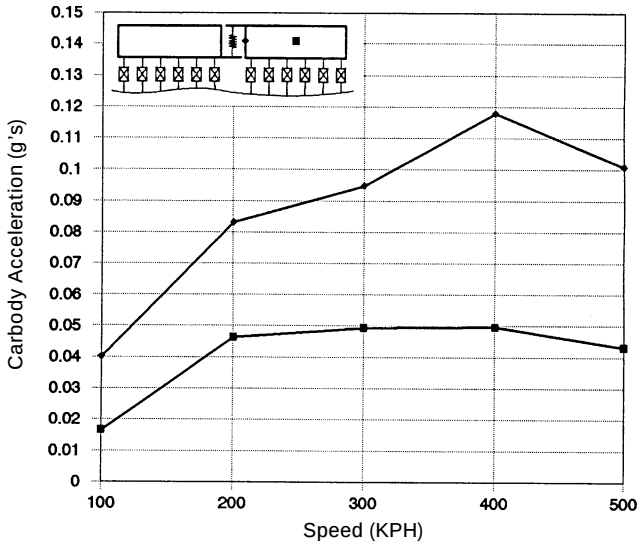

b. 1.0-Hz effective suspension frequency.

Figure 102. Grumman carbody acceleration for vehicle traversing a flexible guideway.

large guideway deflections, in excess of 11 mm. Ride quality could be improved through the introduction of guideway precamber, use of a stiffer guideway, or improved force control characteristics.

Figure 103 shows the maximum gap variations from nominal for the vehicle traversing the flexible guideway with both the 9.1- and 1-Hz suspensions. The stiff suspension follows the guideway more closely. The maximum variation from the nominal gap for the stiff suspension is just over 4 mm, while the maximum variation from nominal is 8 mm for the soft suspension. By following the guideway less closely, the soft suspension is able to provide improved ride quality. Neither suspension uses a large portion of the 50-mm nominal gap.

Figure 104 shows the range of force variations as a function of speed that would be expected for the Grumman vehicle with the 9.1-Hz suspension traveling on the flexible guideway. For the vehicle with the stiff suspension, the analyses tell us that the force between the guideway and the vehicle would become negative, that is, the magnet modules would be required to pull the vehicle down. As the magnet forces cannot become negative, this result says that the magnet modules would become unstable traveling on this guideway. Figure 104 also shows that the force-range capability of the magnet modules would also be exceeded for the 1-Hz suspension, even though the force-range is greatly reduced from the 9.1-Hz suspension. The 50% range of the magnet modules is the *maximum* range at the nominal gap with the vehicle and magnet module control currents at steady state. The actual available force-range may be somewhat less than 50%. If the soft suspension were to be used, it would require a greater force-range capability.

Subsequent to these analyses, Grumman revised its suspension to operate at a nominal 40-mm gap with a steady force variation of ±40% and an intermittent force variation of ±80%. These changes address the concerns noted above. However, time constraints prevented us from analyzing the revised suspension.

Figure 105 shows the forces supporting the vehicle when the vehicle is stationary on a deflected guideway. The vehicle is located over the center of a guideway beam and guideway deflection is approximated as a rectified sine wave with an 11-mm amplitude. Since the vehicle is stationary, the vertical forces between the guideway and vehicle are solely from the effective spring of the force-control characteristic, that is, the force-control characteristic acts as a spring under these conditions. For the stiff suspension, the magnet modules would exceed their force-range capability for the vehicle sitting stationary on such a guideway. In this case, the lead and trail magnet modules carry a load in excess

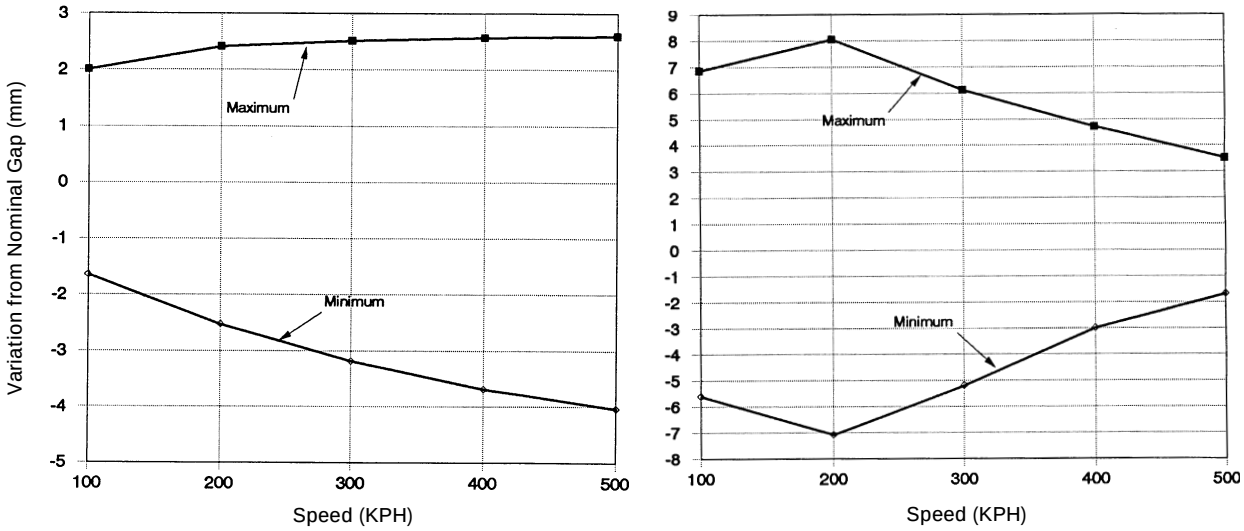

a. 9.1-Hz effective suspension frequency.

b. 1.0-Hz effective suspension frequency.

Figure 103. Grumman gap variation from nominal for vehicle traversing a flexible guideway.

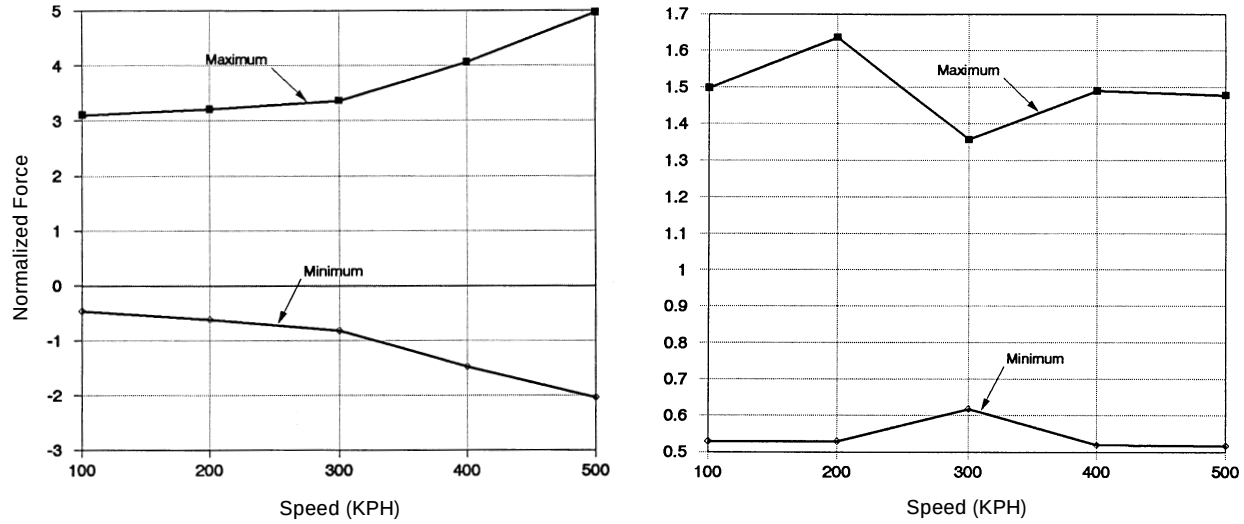

a. 9.1-Hz effective suspension frequency.

b. 1.0-Hz effective suspension frequency.

Figure 104. Guideway force-range acting on the Grumman vehicle.

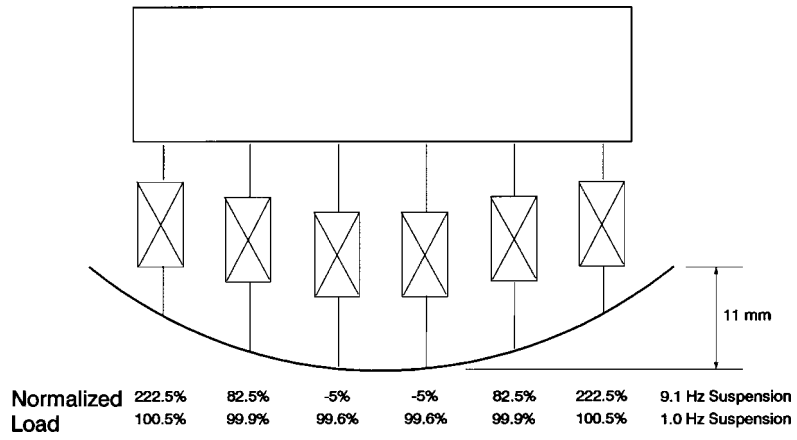

Figure 105. Stationary Grumman vehicle on deflected guideway.

of twice their nominal load, while the two modules closest to the center carry almost no load. For the soft suspension, the variation in force is small, less than 1% from the nominal load. Again, we see that a 1-Hz suspension is superior for the Grumman vehicle. The actual guideway deflection is less than 11 mm when the vehicle is stationary; however, it is greater than 11 mm under some conditions when the vehicle is moving. For the stiff suspension, most of the force variation as the vehicle travels along the guideway is attributable to the effective spring force of the force-control characteristic, in combination with the guideway deflection

The results of the analyses show that the Grumman suspension can be improved, both in terms of the ride quality and in terms of the range of force variations, by reducing its effective natural frequency. However, further improvements in performance may be possible with greater changes in the design of the system. The addition of precamber to the guideway would reduce the effective amplitude of the vertical guideway inputs to the suspension, consequently increasing ride quality and reducing the range of force variations. Revision of the suspension force control characteristic could allow stable independence of the magnet modules and also improve ride quality over poor guideway geometry by taking advantage of the large available gap. It appears that a wide range of force-control characteristics should be possible with the magnet module designed by Grumman, and that it should be capable of a high level of performance (in terms of the ride quality, required guideway geometry and flexibility, and the required force-range capability of the magnet modules). With further work, this innovative suspension would likely achieve its high potential.

Magneplane. Time constraints prevented a thorough analysis of the Magneplane vehicle. We discuss its features only qualitatively here.

The Magneplane suspension is semi-active; that is, only the damping in the suspension is controlled while the effective spring stiffness of the magnetic suspension is not controlled. The optimum strategy for such a suspension is "skyhook" damping. Conceptually, this strategy connects one end of the damper to a (vertically) fixed reference and the other end to the vehicle. (Conventional passive damping, in essence, connects one end of the damper to the guideway and the other end to the vehicle.) The potential advantage of active or semi-active suspensions is a relaxation of the guideway geometry and flexibility requirements for acceptable ride quality.

The Grumman suspension is fully active and its steady-state behavior is similar to a semi-active suspension with a skyhook damping. The Magneplane suspension is semi-active, rather than fully active, and the Magneplane vehicle is suspended only at two locations (essentially a bogie-type vehicle) rather than suspended continuously along its length such as TR07 and Grumman. Because of this, the steady-state behavior of the Magneplane vehicle will be somewhat worse than the steady-state behavior of the Grumman vehicle. That is, the comparable carbody accelerations shown in Figure 101 for the Grumman vehicle will be somewhat greater for the Magneplane vehicle.

Viability issues

Reduced guideway requirements have become a principal issue in developing maglev vehicle suspensions. Guideway construction and maintenance add greatly to the life-cycle cost of a maglev system. Any reduction in these costs could favorably influence the decision to build such a system. This assessment has primarily focused on determining the guideway requirements for proposed maglev systems.

Increased gap sizes have been proposed as a way of allowing reduced guideway requirements. However, the analyses of the dynamic performance of TR07 and the Foster-Miller vehicle, both of which use stiff primary and passive secondary suspensions, indicate that ride quality dictates the minimum level of guideway geometry and stiffness. Consequently, increasing the gap between the vehicle and the guideway will not reduce the guideway's geometry requirements for systems with stiff primary suspensions and passive secondary suspensions.

To relax guideway geometry and stiffness requirements and take advantage of a large gap, significant improvements in vehicle suspensions are required. Specifically, active suspensions are necessary. The Grumman and Magneplane vehicles have unconventional suspensions. They combine the functions of conventional primary and secondary suspensions into one that has actively controlled elements. These suspensions have the potential to capitalize on larger magnet gaps; however, their implementation details will determine how well they achieve this potential. Our analysis showed that the Grumman vehicle, as designed, performs no better than a vehicle

equipped with a well-tuned conventional suspension. Although no detailed analysis was done, it is likely that the Magneplane SCD will not perform as well as the Grumman SCD, primarily because the Magneplane vehicle is a bogie-type vehicle and the Grumman vehicle is a distributed-support-type vehicle.

Clearly, active suspensions warrant further investigation. Such suspensions hold significant potential to maintain adequate levels of safety and ride comfort over relatively rough and flexible (i.e., less expensive) guideways. Properly done, they could be critical to efforts to reduce maglev guideway, and hence system, costs.

Preview control and adaptive control of vehicle suspensions were not explored at all, and feedback control was not explored thoroughly, by the SCD contractors. Research is still needed to make optimal maglev vehicle suspensions.

3.3 SYSTEM-LEVEL VERIFICATION

3.3.1 System performance simulation*

Objectives

Computer simulation of maglev system-level performance transforms technological characteristics (vehicle weight, motor thrust, tilting capability, etc.) into system characteristics that affect ridership (trip time, ride comfort, service frequency, etc.) and costs (fleet size, energy consumption, etc.). Thus, system simulation offers a way to evaluate each concept's ability to serve U.S. markets. It also offers a design tool for developing cost-effective U.S. maglev concepts.

We simulated the performance of TR07 and the four SCDs over two hypothetical routes: 1) a 40-km straight and flat route, and 2) a specially prepared severe segment test (SST). The performance requirement for these simulations was to minimize trip time within the constraints of ride comfort and a 134-m/s maximum speed. The straight and flat route allowed easy comparison of thrust and resistance differences among systems, while the SST highlighted performance differences along route segments broadly representative of common U.S. terrain.

The Government provided the SCD contractors with the SST route specifications at the onset of the contracts. They used this route to estimate system performance and costs. While the SST does not represent the route characteristics of any particular U.S. corridor, average results for real U.S. corridors compare well with those for the SST (using the simulation method described in Martin-Marietta 1992). Thus, we may view the SST results as representative, on average, of U.S. routes. The simulations use as inputs the SST route specifications, ride-comfort constraints, and vehicle and LSM performance data. Outputs include trip time, energy usage, and speed profiles.

A primary objective of these simulations was to compare the performance of the U.S. maglev systems with TR07. Transrapid designed TR07 to be an on-line-station system, connecting closely spaced population centers such as are found in Europe. By comparison, the SCDs focused on systems capable of more frequent service to off-line stations with smaller population densities. Thus, a system-level comparison between TR07 and the SCDs supports a key focus of the NMI program, namely to assess the capability of U.S. industry to improve on available foreign technology. Note that TGV is unable to climb the steep grades included in the SST; we, therefore, did not simulate its performance.

Severe segment test route

The Government developed the SST to permit evaluation of each system's performance along a common route. Figure 106 shows, in graphical form, the 800-km route and its four on-line stations. It consists of three sections. The first 400 km between terminal no. 1 (the origin) and terminal no. 2 is a section of guideway with many closely spaced curves. The vehicles must slow down through most of these curves to meet the ride-comfort criteria. This section is representative of rugged terrain such as may be found along the New York State Thruway. Between terminal no. 2 and terminal no. 3 (at 470 km), the curves are less severe and are separated by greater distances. This is more representative of terrain with rolling hills. The last section (terminal no. 3 to 4) is a straight line section that allows a very high average speed. Compound horizontal and vertical curves occur throughout the SST route. Grades vary over the route from –10% to +10%.

The SST route is described by a horizontal profile and a vertical profile. The horizontal profile specifies the distance along tangents between points of intersection (PI), and specifies the radius of curvature (R_h) and the change in azimuth (I) at

* Written by Dr. James H. Lever, CRREL, Frank L. Raposa, Consulting Engineer, and George Anagnostopoulos, U.S. Department of Transportation.

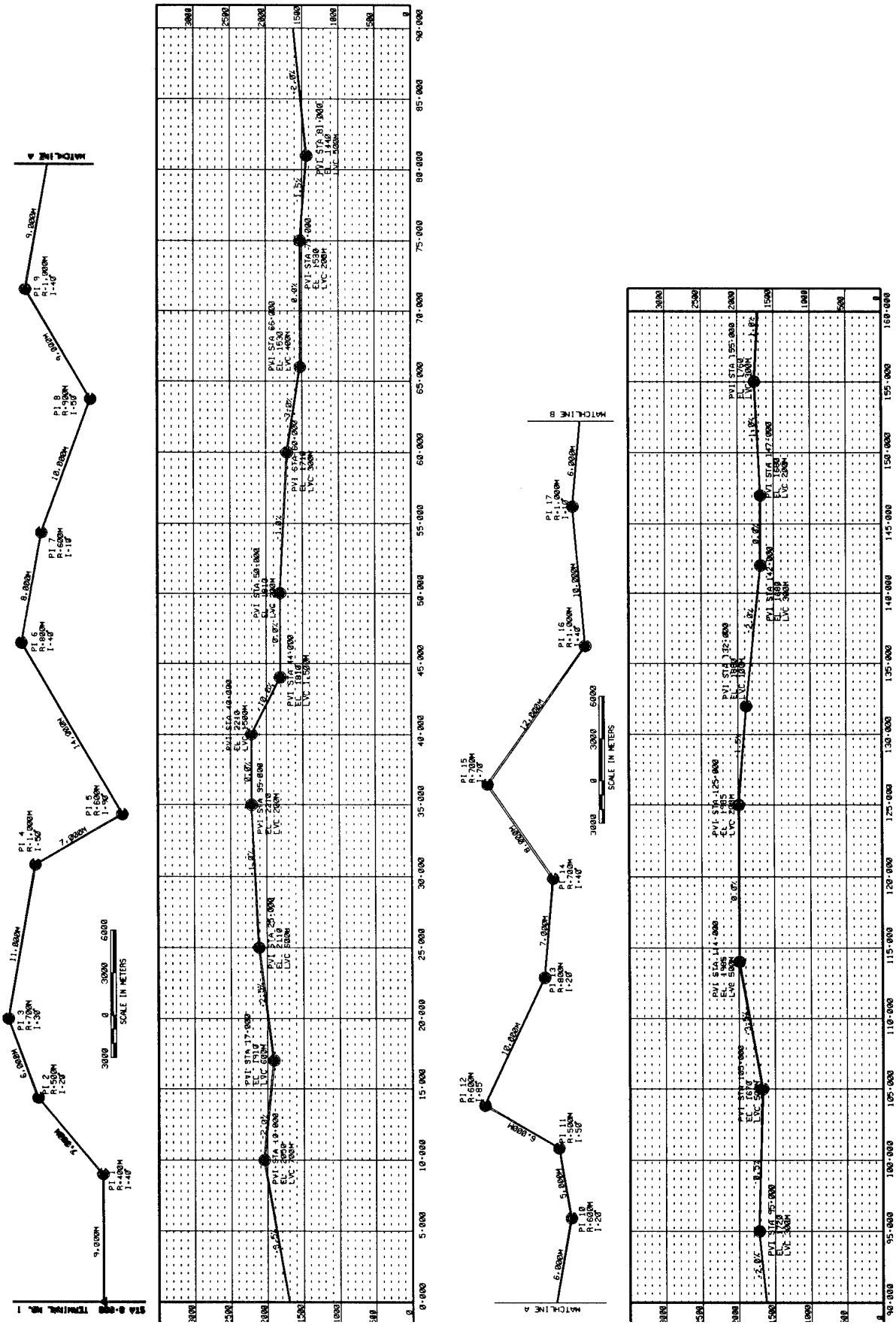

a. 0–160 km.

Figure 106. Severe segment test (SST) route.

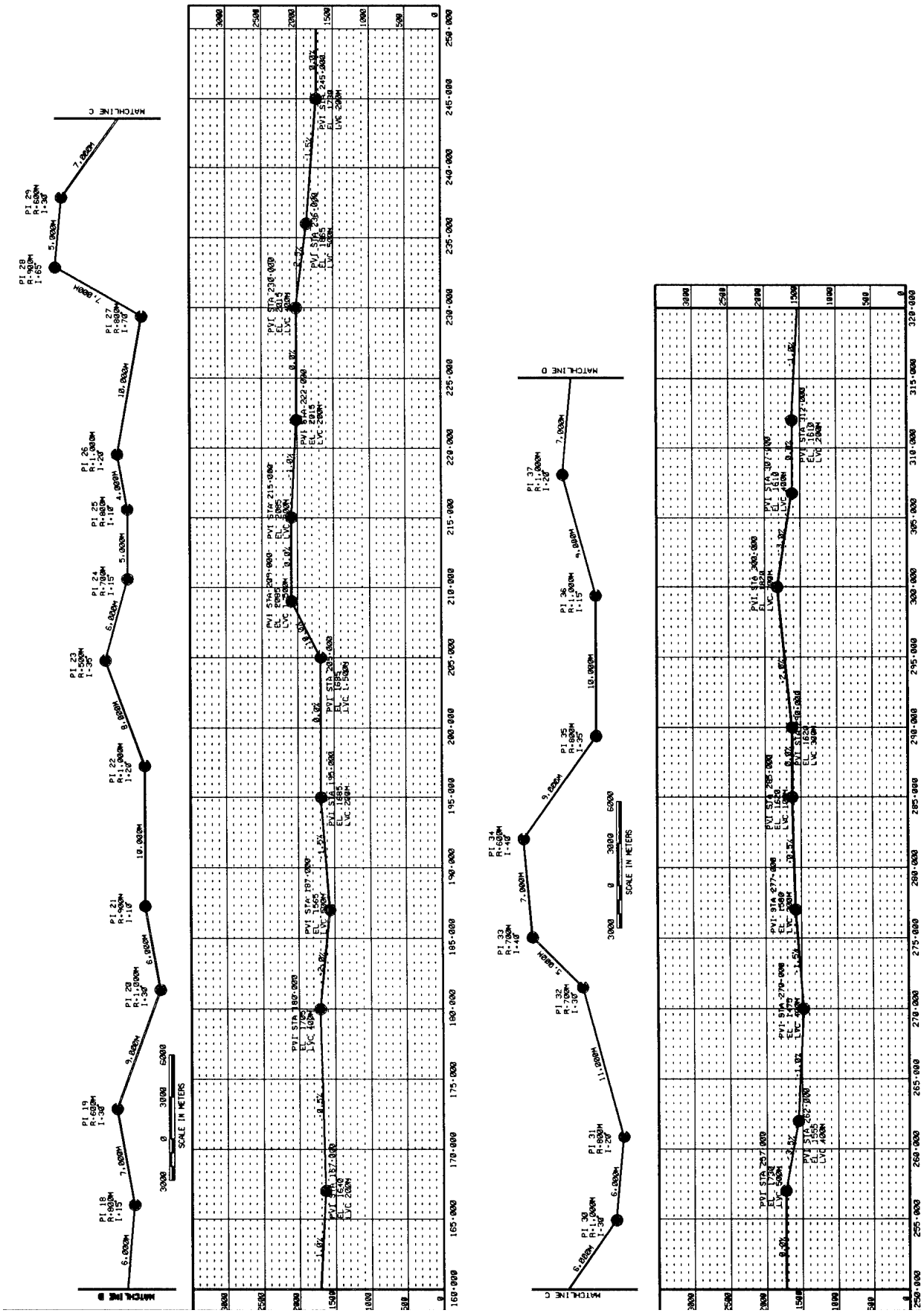

b. 160–320 km.

Figure 106 (cont'd)

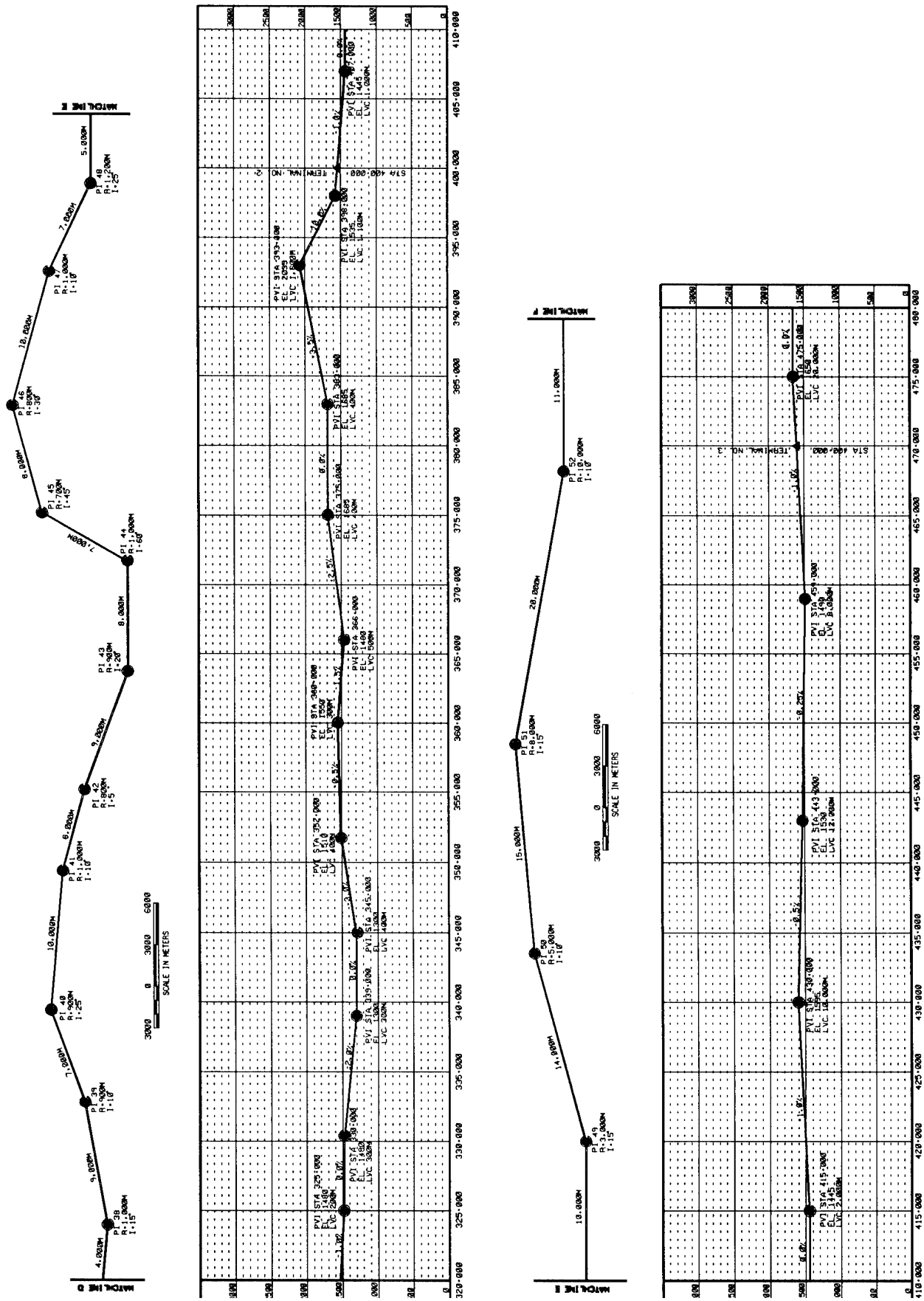

c. 320–480 km.

Figure 106 (cont'd). Severe segment test (SST) route.

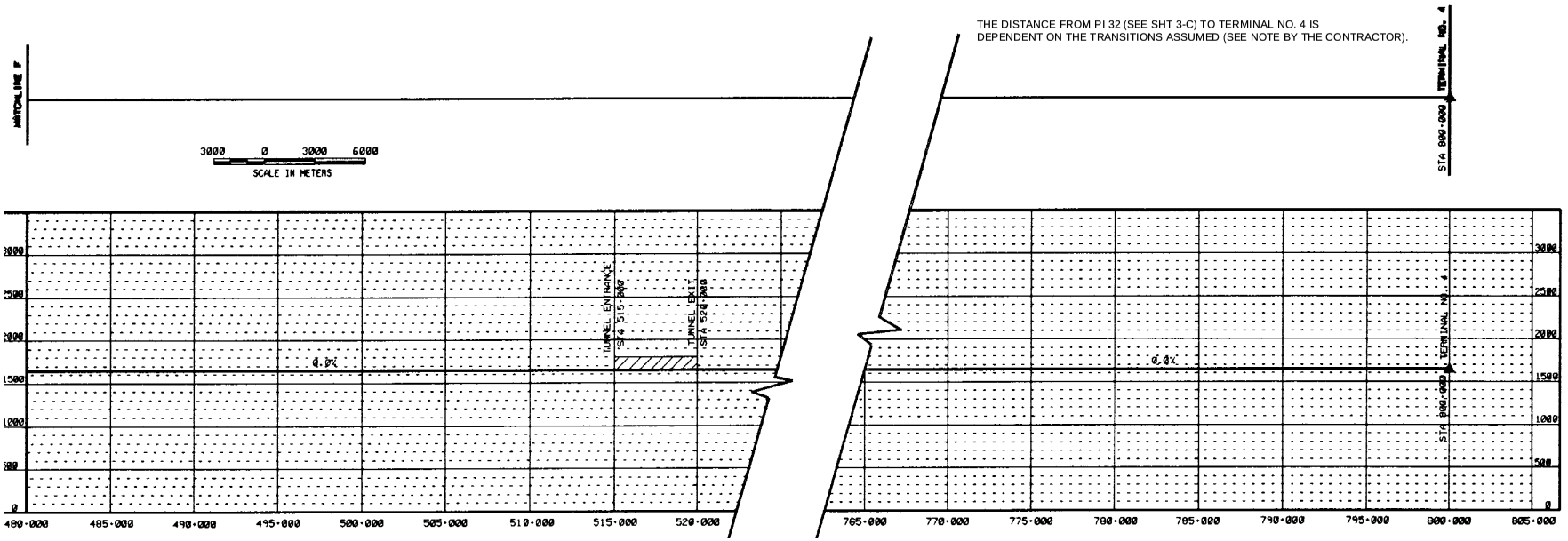

Notes:

1. Numerical data are based on the International System of Units (SI). Stationing, distances, and elevations shown are in meter units.
2. The alignment shown is for guideway centerline.
3. The contractor is restricted to the horizontal and vertical curve data indicated but shall assume transitions as required to complement system performance.
4. The vertical curve data provided are based on equal-distance tangents.
5. The elevations indicated in profile are provided for computation of grades only and are not referenced to a specific vertical datum. The contractor shall assume an atmospheric pressure of one atmosphere at all points along the guideway centerline.
6. Acronyms are defined as follows:

PI = Point of intersection of tangents
R = Radius of curvature
I = Deflection angle between tangents
LVC = Length of vertical curve
PVI = Point of vertical intersection of tangents

d. 480–805 km.

Figure 106 (cont'd)

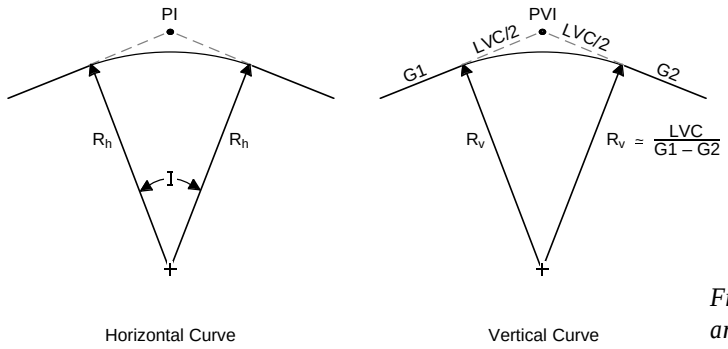

Figure 107. Notation for horizontal and vertical curves for SST route.

each point of intersection. The vertical profile specifies the distance along tangents between points of vertical intersection (PVI), and for each PVI, the elevation, the entering and exiting grades (G1 and G2), and the length of vertical curve (LVC) measured along tangents. Figure 107 shows these curve details. Note that vertical radius of curvature (RV) approximately equals LVC / (G1–G2). The SST consists of 52 PI's and 56 PVI's, of which six are combined horizontal and vertical curves. The SST instructions did not specify the proportion of total turning angle or grade change within the transition sections leading to or away from a curve. However, the vehicle must transit at least a portion of the curve at the given curve radius. Also, the vehicle must stop at each terminal before continuing along the route. We did not simulate the 5-km-long tunnel in segment 3 of the SST because its effects should be small and essentially independent of which system is used.

Table 39. Ride comfort guidelines for curving performance (maximum values for event, i.e., spiral or curve).

	Design goal	*Minimum requirements*	*Seated–belted*
Lateral curves			
Bank angle (deg)	24	30	45
Roll rate (deg / s)	5		10
Lateral (g's)	0.1	0.16	0.2
Roll acceleration (deg / s^2)	15		
Vertical curves			
Vertical (up) (g's)	0.05	0.1	0.1
Vertical (down) (g's)	0.2	0.3	0.4
Acceleration and braking			
Normal (g's)	0.16	0.2	0.6
Vector combinations			
Lateral / longitudinal (g's)	0.2	0.3	0.6
Lateral / vertical (g's)	0.2	0.3	0.4
Total (g's)	0.24	0.36	0.6
Jerk (g's/s filtered at 0.3 Hz) or Jolt (peak to peak g's in 1 s)			
Lateral	0.07	0.25	0.25
Vertical	0.1	0.3	0.3
Longitudinal	0.07	0.25	0.25

Ride comfort guidelines

The motion of a maglev vehicle along a practical route will subject the passengers to a variety of motions arising from acceleration, curving, and braking. Ride comfort guidelines describe the set of maximum rigid-body motions acceptable to passengers under various conditions. On 16 December 1991, a Ride Quality Workshop was held that developed ride comfort guidelines for the SCD contractors to use in their study of the SST. Table 39 summarizes the three sets of guidelines established (see also Appendix A). Design goal (DG) criteria were based on ride comfort values known to be acceptable to passengers when standing and walking in a moving vehicle. Minimum requirement (MR) criteria reflect marginally acceptable conditions for standing and walking passengers. Seated–belted (SB) criteria represent motions acceptable for passengers that are seated and belted. We conducted system simulations only for the DG criteria. These represent the most conservative guidelines in terms of the performance of the vehicle and the comfort of the passengers.

System simulator: SSTSIM

The simulation software, SSTSIM, solves the time-domain equations of motion for a given vehicle at each point along the guideway. It uses two sets of inputs: 1) the SST route characteristics (location of each curve or terminal, entering and exiting grades, curve radius, and maximum allowable speed), and 2) the vehicle–LSM dynamic characteristics (vehicle mass, speed-dependent vehicle

resistance, LSM thrust, and LSM efficiency). Ride comfort criteria restrict the allowable longitudinal acceleration and braking rates and establish the maximum curve speeds.

Local coordinates. The ride comfort criteria refer to the local coordinate system of seated passengers. Local guideway grade, thus, influences allowable longitudinal accelerations. For example, the DG longitudinal acceleration limit is 0.16 g. This means that a vehicle can only accelerate up a 10% grade at 0.06 g to remain within the comfort limit. Conversely, the vehicle can accelerate down a 10% grade at 0.26 g without subjecting the passengers to more than 0.16 g. The influence is reversed for vehicle braking on grades. All vehicles simulated can brake at the local maximum rate dictated by ride comfort. However, net LSM thrust determines the achievable forward acceleration unless this value exceeds the local ride comfort limit.

Ride comfort criteria for lateral and vertical accelerations also refer to the local coordinate system. The SCDs use a combination of guideway superelevation (or cant) and vehicle tilt to increase curving speeds while remaining within these ride comfort limits. Tilt also gives the system the flexibility of stopping in a curve without exceeding acceptable ride-quality constraints.

Figure 108 shows a vector diagram for determining the local lateral and vertical accelerations in a compound horizontal and vertical curve. A force balance yields

$$A_{\text{lat}} = \frac{v^2}{gR_{\text{h}}}\cos\vartheta - \left(1 + \frac{v^2}{gR_{\text{v}}}\right)\sin\vartheta \qquad (15)$$

$$A_{\text{vert}} = \frac{v^2}{gR_{\text{h}}}\sin\vartheta + \left(1 + \frac{v^2}{gR_{\text{v}}}\right)\cos\vartheta \qquad (16)$$

where A_{lat} = local lateral acceleration (g's)
A_{vert} = local vertical acceleration (g's)
v = vehicle speed through curve
g = gravitational acceleration
R_{h} = horizontal radius of curvature
R_{v} = vertical radius of curvature (positive for upward curvature or trough)
ϑ = vehicle bank angle.

Primary ride comfort criteria. Equations 15 and 16 directly establish the maximum speeds allowable at the minimum radius in horizontal, vertical, and combined curves. Vector combinations of

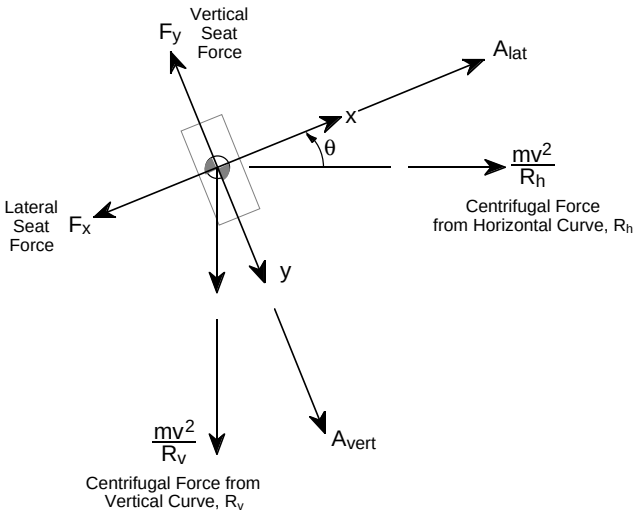

Figure 108. Lateral and vertical acceleration vectors.

accelerations, roll rates, roll accelerations, and jerks (changes in accelerations) can be similarly calculated. To minimize trip time, the vehicle should operate on the mathematical surface bounding the allowable motions. For the DG ride comfort level, a few key criteria actually dictate allowable vehicle motion, namely: lateral acceleration in horizontal or combined curves, vertical acceleration in vertical curves, and longitudinal acceleration–braking and longitudinal jerk during speed changes.

The lateral acceleration criterion establishes a speed limit v_{l} at the minimum radius in a horizontal curve via eq 15. Local vertical acceleration also occurs in a tilting vehicle on a horizontal curve. However, for DG and MR criteria, the speed limit from this cause is higher than v_{l}. Furthermore, transiting the given curve radius at v_{l} ensures that the vehicle satisfies the limits on combined lateral–vertical and total accelerations for DG and MR criteria.

As noted, the SST did not specify the length or shape of curve transition sections (called spirals for horizontal curves). Thus, the design of these sections can accommodate the secondary ride comfort criteria (roll rate, roll acceleration, and lateral and vertical jerks). In addition, it should be possible to vary radius and turning angle along the spiral so that the longitudinal acceleration–braking criterion always dictates the speed profile. A curve offset described by a fourth-degree polynomial appears to meet these requirements. That is, v_{l}, longitudinal acceleration–braking, and longitudinal jerk constitute the DG and MR ride comfort limits for horizontal curves.

The upward or downward vertical-acceleration criterion establishes a speed limit v_v at the minimum radius in a vertical curve via eq 16. Because vehicle tilting yields a negligible performance benefit in a vertical curve, v_v is system independent. For DG ride comfort criteria, v_v is less than 134 m/s for only 23 vertical curves in the SST (excluding combined horizontal–vertical curves) and all of these are cresting cases. The local grades entering and leaving vertical curves cause negligible reductions in the allowable vertical accelerations (applied in local coordinates). The DG and MR criteria for allowable total acceleration are met for all cresting curves by simply meeting the corresponding vertical acceleration limits. Because the vehicles can transit all trough curves at 134 m/s, they experience no additional longitudinal accelerations and thus also meet the total acceleration limits. As with horizontal curves, entry and exit guideway transitions can accommodate vertical jerk criteria. Therefore, v_v, longitudinal acceleration–braking, and longitudinal jerk constitute the DG and MR ride comfort limits for vertical curves.

Equations 15 and 16 can be used to compute the accelerations experienced in the six combined horizontal–vertical curves of the SST route. However, the vertical radii of curvature are all much longer than the horizontal radii, so that acceleration components resulting from the vertical radii can be neglected. If the vehicle transits the curve at speed v_l, computed as if the curve had only a horizontal radius, it easily satisfies the total acceleration criteria. Therefore, v_l, longitudinal acceleration–braking, and longitudinal jerk approximate the DG and MR ride comfort limits for combined curves.

SSTSIM algorithm. Use of the aforementioned set of primary ride comfort criteria simplifies the algorithm required for the simulations of interest here—vehicles traversing the SST route under DG ride comfort criteria. For each system, we computed the speed gates (i.e., the set of maximum vehicle speeds) for the horizontal and combined curves v_{li} from eq 15 using the maximum vehicle bank angle and neglecting the term for vertical curvature. We then combined these with the speed gates for the vertical curves v_{vi}, from eq 16 using zero bank angle, and the required terminal stops, both of which are system independent. Table 40 shows the speed gate file for the SST; cruise speed (134 m/s) is the target speed between speed gates. This speed profile, combined with the longitudinal acceleration–braking limit of 0.16 g (modified by local guideway grade) and the longitudinal jerk limit of 0.07 g/s, establish the kinematic constraints for the SST (maximum speed, acceleration, braking rate, and jerk allowed at each position or time). We set gravitational acceleration g equal to 9.80 m/s^2, a value appropriate for most of the U.S.

Because the performance objective is to minimize trip time, all vehicles accelerate at the system's maximum LSM thrust for that speed, and braking and roll-off and roll-on jerks occur at the ride comfort limits. At each time step, the algorithm computes the distance required to brake from the current speed to the next speed gate. If this distance is less than the distance available, the vehicle follows the local kinematic constraints (acceleration to, or continued motion at, cruise speed); otherwise, the vehicle begins to brake for the speed gate. The algorithm automatically handles acceleration through a speed gate by including a roll-off to zero acceleration, one time step at the gate speed, and roll-on back to maximum acceleration. For a few cases where a low-speed gate closely follows a high-speed gate, the braking path to the low-speed gate establishes the required brake point. In these cases, the vehicle brakes continuously through the high-speed gate at a speed typically well below the gate speed.

Energy consumption during accelerations (including associated roll-on and roll-off jerks) is calculated at maximum-thrust conditions. Energy consumption during cruise periods is calculated for normal-thrust conditions (LSM thrust equal to vehicle resistance); energy consumption is zero during braking. Although regenerative braking is possible with most maglev concepts, we did not include it here. Regenerative braking would lower energy consumption along the SST. SSTSIM calculates energy consumption for each system at the outputs of the converter stations (i.e., the inputs to the LMSs). For subsequent calculations of system energy intensity, based on energy supplied from an electric utility, we manually applied speed-independent converter station efficiencies to the SSTSIM results.

Simulation results (speed profile, trip time, and energy consumption) were not sensitive to time steps between 0.1–0.01 s, and we used 0.1 s for most runs. Overshoots of speed gates were typically less than 0.05 m/s and 10 m, adequate for these simulations. The algorithm reset the vehicle at the gate speed and position to remove any cumulative advantage of overshoots.

SSTSIM does not design guideway curves or

Table 40. Speed gate file for the SST route.

Point of intersection (neg. = PVI)	*Station (m)*	*Speed gate (m/s) (12° bank)*	*Speed gate (m/s) SCDs (24° bank)*	*Length of vertical curve (m)*	*Entering grade, G1*	*Exiting grade, G2*
Terminal 1	0.0	0.0	0.0	0.0	0.000	0.035
1.0000	9,000.0	35.2	46.6	—	0.035	0.035
–1.0000	10,000.0	79.0	79.0	700.0	0.035	–0.020
2.0000	16,000.0	39.3	52.1	—	–0.020	–0.020
–2.0000	17,000.0	161.7	161.7	600.0	–0.020	0.025
3.0000	22,000.0	46.5	61.7	—	0.025	0.025
–3.0000	25,000.0	140.0	140.0	600.0	0.025	0.010
4.0000	33,000.0	55.5	73.7	—	0.010	0.010
–4.0000	35,000.0	99.0	99.0	200.0	0.010	0.000
5.0000	40,000.0	43.0	57.1	1500.0	0.000	–0.100
–6.0000	44,000.0	171.5	171.5	1500.0	–0.100	0.000
–7.0000	50,000.0	99.0	99.0	200.0	0.000	–0.010
6.0000	54,000.0	49.7	65.9	—	–0.010	–0.010
–8.0000	60,000.0	85.7	85.7	300.0	–0.010	–0.030
7.0000	62,000.0	43.0	57.1	—	–0.030	–0.030
–9.0000	66,000.0	161.7	161.7	400.0	–0.030	0.000
8.0000	72,000.0	52.7	69.9	—	0.000	0.000
–10.000	75,000.0	80.8	80.8	200.0	0.000	–0.015
9.0000	81,000.0	55.5	73.7	500.0	–0.015	0.020
–12.000	95,000.0	76.7	76.7	300.0	0.020	–0.005
10.000	96,000.0	43.0	57.1	—	–0.005	–0.005
11.000	101,000.0	39.3	52.1	—	–0.005	–0.005
–13.000	105,000.0	156.5	156.5	500.0	–0.005	0.035
12.000	107,000.0	43.0	57.1	—	0.035	0.035
–14.000	114,000.0	83.7	83.7	500.0	0.035	0.000
13.000	117,000.0	49.7	65.9	—	0.000	0.000
14.000	124,000.0	46.5	61.7	—	0.000	0.000
–15.000	125,000.0	80.8	80.8	200.0	0.000	–0.015
15.000	132,000.0	46.4	61.7	100.0	–0.015	–0.020
–17.000	142,000.0	171.5	171.5	300.0	–0.020	0.000
16.000	144,000.0	55.5	73.7	—	0.000	0.000
–18.000	147,000.0	198.0	198.0	200.0	0.000	0.010
17.000	154,000.0	55.5	73.7	—	0.010	0.010
–19.000	155,000.0	85.7	85.7	300.0	0.010	–0.010
18.000	166,000.0	49.7	65.9	—	–0.010	–0.010
–20.000	167,000.0	161.7	161.7	200.0	–0.010	0.005
19.000	173,000.0	43.0	57.1	—	0.005	0.005
–21.000	180,000.0	88.5	88.5	400.0	0.005	–0.020
20.000	182,000.0	55.5	73.7	—	–0.020	–0.020
–22.000	187,000.0	167.3	167.3	500.0	–0.020	0.015
21.000	188,000.0	52.7	69.9	—	0.015	0.015
–23.000	195,000.0	80.8	80.8	200.0	0.015	0.000
22.000	198,000.0	55.5	73.7	—	0.000	0.000
–24.000	205,000.0	171.5	171.5	1500.0	0.000	0.100
23.000	206,000.0	39.3	52.1	—	0.100	0.100
–25.000	209,000.0	85.7	85.7	1500.0	0.100	0.000
24.000	212,000.0	46.5	61.7	—	0.000	0.000
–26.000	215,000.0	99.0	99.0	200.0	0.000	–0.010
25.000	217,000.0	49.7	65.9	—	–0.010	–0.010
26.000	221,000.0	55.5	73.7	—	–0.010	–0.010
–27.000	222,000.0	198.0	198.0	200.0	–0.010	0.000
–28.000	230,000.0	88.5	88.5	400.0	0.000	–0.025
27.000	231,000.0	49.7	65.9	—	–0.025	–0.025
–29.000	236,000.0	313.0	313.0	500.0	–0.025	–0.015
28.000	238,000.0	52.7	69.9	—	–0.015	–0.015
29.000	243,000.0	43.0	57.1	—	–0.015	–0.015
–30.000	245,000.0	161.7	161.7	200.0	–0.015	0.000
30.000	256,000.0	55.5	73.7	—	0.000	0.000
–31.000	257,000.0	83.7	83.7	500.0	0.000	–0.035
31.000	262,000.0	49.7	65.9	400.0	–0.035	–0.010
–33.000	270,000.0	177.1	177.1	400.0	–0.010	0.015
32.000	273,000.0	46.5	61.7	—	0.015	0.015

Table 40 (cont'd). Speed gate file for the SST route.

Point of intersection (neg. = PVI)	*Station (m)*	*Speed gate (m/s) (12° bank)*	*Speed gate (m/s) SCDs (24° bank)*	*Length of vertical curve (m)*	*Entering grade, G1*	*Exiting grade, G2*
–34.000	277,000.0	99.0	99.0	200.0	0.015	0.005
33.000	278,000.0	46.5	61.7	—	0.005	0.005
34.000	285,000.0	43.0	57.1	100.0	0.005	0.000
–36.000	290,000.0	171.5	171.5	300.0	0.000	0.020
35.000	294,000.0	49.7	65.9	—	0.020	0.020
–37.000	300,000.0	82.8	82.8	700.0	0.020	–0.030
36.000	304,000.0	55.5	73.7	—	–0.030	–0.030
–38.000	307,000.0	161.7	161.7	400.0	–0.030	0.000
–39.000	312,000.0	99.0	99.0	200.0	0.000	–0.010
37.000	313,000.0	55.5	73.7	—	–0.010	–0.010
38.000	324,000.0	55.5	73.7	—	–0.010	–0.010
–40.000	325,000.0	198.0	198.0	200.0	–0.010	0.000
–41.000	330,000.0	85.7	85.7	300.0	0.000	–0.020
39.000	333,000.0	52.7	69.9	—	–0.020	–0.020
–42.000	339,000.0	171.5	171.5	300.0	–0.020	0.000
40.000	340,000.0	52.7	69.9	—	0.000	0.000
–43.000	345,000.0	161.7	161.7	400.0	0.000	0.030
41.000	350,000.0	55.5	73.7	—	0.030	0.030
–44.000	352,000.0	88.5	88.5	400.0	0.030	0.005
42.000	356,000.0	49.7	65.9	—	0.005	0.005
–45.000	360,000.0	85.7	85.7	300.0	0.005	–0.015
43.000	365,000.0	52.7	69.9	—	–0.015	–0.015
–46.000	366,000.0	156.5	156.5	500.0	–0.015	0.025
44.000	373,000.0	55.5	73.7	—	0.025	0.025
–47.000	375,000.0	88.5	88.5	400.0	0.025	0.000
45.000	380,000.0	46.5	61.7	—	0.000	0.000
–48.000	383,000.0	149.7	149.7	400.0	0.000	0.035
46.000	388,000.0	49.7	65.9	—	0.035	0.035
–49.000	393,000.0	76.2	76.2	1600.0	0.035	–0.100
47.000	398,000.0	55.5	73.7	1100.0	–0.100	–0.010
Terminal 2	400,000.0	0.0	0.0	—	–0.010	–0.010
48.000	405,000.0	60.8	80.8	—	–0.010	–0.010
–51.000	407,000.0	442.7	442.7	1000.0	–0.010	0.000
–52.000	415,000.0	626.1	626.1	2000.0	0.000	0.010
49.000	420,000.0	96.2	127.7	—	0.010	0.010
–53.000	430,000.0	571.5	571.5	10,000.0	0.010	–0.005
50.000	434,000.0	124.2	164.9	—	–0.005	–0.005
–54.000	443,000.0	3067.2	3067.2	12,000.0	–0.005	–0.002
51.000	449,000.0	157.1	208.5	—	–0.002	–0.002
–55.000	459,000.0	1120.0	1120.0	8000.0	–0.002	0.010
52.000	469,000.0	175.6	233.1	—	0.010	0.010
Terminal 3	470,000.0	0.0	0.0	—	0.010	0.010
–56.000	475,000.0	989.9	989.9	20,000.0	0.010	0.000
Terminal 4	800,000.0	0.0	0.0	—	0.000	0.000

transition spirals because these relate to secondary ride comfort criteria neglected in our approximations. Consequently, SSTSIM does not calculate guideway offsets (i.e., ROW requirements). However, these are not strongly system dependent. The SST requirement of traversing a portion of the curve at the specified minimum radius is met by establishing the speed gates, as described above.

Thrust, efficiency, and resistance. Section 3.2.2 presents our analysis of the linear synchronous motors used by TR07 and the four SCDs. The tables in that section show LSM thrust and efficiency vs. vehicle speed for the two conditions of interest here: maximum thrust and normal thrust. SSTSIM uses these data in a series of lookup tables to determine the LSM thrust and efficiency at each time step, using linear interpolation between the speeds tabulated. The tables in section 3.2.2 also show calculated vehicle resistance (air and magnetic drag) vs. speed. For completeness, the resistance lookup tables used in SSTSIM also include drag induced by the linear generators used to transfer hotel power (significant only at speeds below about 50 m/s). Table 41 shows the SSTSIM

Table 41. LSM and resistance data used in SSTSIM.

Condition	*Speed (m/s)*	*Thrust (kN)*	*Efficiency*	*Resistance (kN)*
	a. TR07. Vehicle mass is 106,000 kg.			
Cruise	134.00	61.800	0.88000	61.800
Maximum thrust	0.0000	110.20	0.0010000	10.300
	1.0000	110.20	0.030000	10.300
	10.000	110.20	0.23000	10.800
	15.000	110.20	0.31000	11.300
	20.000	110.20	0.38000	11.900
	30.000	110.20	0.48000	13.700
	40.000	110.20	0.55000	15.800
	50.000	110.20	0.60000	16.900
	60.000	110.20	0.64000	19.100
	60.500	109.80	0.65000	19.300
	70.000	101.40	0.70000	22.400
	80.000	94.000	0.74000	26.700
	90.000	87.600	0.77000	31.800
	100.00	82.200	0.80000	37.700
	110.00	77.400	0.83000	44.200
	120.00	73.200	0.85000	51.200
	130.00	69.400	0.86000	58.700
	134.00	68.000	0.87000	61.800
	b. Bechtel. Vehicle mass is 63,300 kg.			
Cruise	134.0	50.9	0.942	50.9
Maximum thrust	0.0	143.0	0.001	10.5
	1.0	143.0	0.030	10.8
	10.0	143.0	0.306	13.2
	15.0	143.0	0.398	14.4
	20.0	143.0	0.468	15.4
	30.0	143.0	0.569	17.3
	40.0	143.0	0.638	18.9
	50.0	143.0	0.688	20.5
	60.0	143.0	0.726	22.2
	70.0	143.0	0.755	24.1
	80.0	143.0	0.779	26.4
	90.0	143.0	0.799	29.1
	100.0	143.0	0.815	32.5
	110.0	143.0	0.829	36.7
	111.8	143.0	0.831	37.6
	120.0	136.6	0.847	41.9
	130.0	129.4	0.863	48.1
	134.0	126.8	0.869	50.9
	c. Foster-Miller. Vehicle mass is 72,700 kg.			
Cruise	134.0	48.0	0.964	48.0
Maximum thrust	0.0	125.8	0.006	7.2
	10.0	125.8	0.920	7.6
	15.0	125.8	0.940	10.3
	20.0	125.8	0.950	13.7
	26.0	125.8	0.955	15.4
	30.0	125.8	0.956	15.7
	40.0	125.8	0.957	17.4
	50.0	125.8	0.955	19.2
	60.0	125.8	0.952	21.3
	70.0	125.8	0.948	23.5
	80.0	125.8	0.944	26.1
	83.5	125.8	0.943	27.1
	90.0	117.0	0.943	29.0
	100.0	105.5	0.944	32.4
	110.0	95.9	0.945	36.3
	120.0	88.2	0.945	40.7
	130.0	81.4	0.946	45.8
	134.0	79.0	0.946	48.0
	d. Grumman. Vehicle mass is 61,200 kg.			
Cruise	134.0	31.0	0.820	31.0
Maximum thrust	0.0	60.0	0.001	4.1
	1.0	60.0	0.015	4.1
	10.0	60.0	0.149	4.3
	15.0	60.0	0.208	4.5
	20.0	60.0	0.260	4.7
	25.0	60.0	0.305	5.1
	30.0	60.0	0.345	5.5
	40.0	60.0	0.412	6.7
	50.0	60.0	0.467	8.1
	60.0	60.0	0.513	9.9
	70.0	60.0	0.551	11.5
	80.0	60.0	0.584	13.5
	90.0	60.0	0.612	16.0
	100.0	60.0	0.637	18.8
	110.0	60.0	0.659	22.0
	120.0	60.0	0.678	25.5
	130.0	60.0	0.695	29.4
	134.0	60.0	0.701	31.0
	e. Magneplane. Vehicle mass is 48,000 kg.			
Cruise	134.0	37.6	0.884	37.6
Maximum thrust	0.0	150.0	0.000	35.1
	1.0	150.0	0.012	35.1
	10.0	150.0	0.124	35.2
	15.0	150.0	0.175	35.3
	20.0	150.0	0.221	35.5
	30.0	150.0	0.299	36.0
	32.0	150.0	0.312	57.3
	35.0	150.0	0.332	54.9
	40.0	150.0	0.362	51.4
	45.0	150.0	0.390	48.3
	50.0	150.0	0.415	47.9
	52.0	144.2	0.434	46.5
	60.0	125.0	0.505	41.9
	70.0	107.1	0.582	38.1
	80.0	93.8	0.645	35.9
	90.0	83.3	0.697	34.8
	100.0	75.0	0.739	34.4
	110.0	68.2	0.774	34.7
	120.0	62.5	0.803	35.6
	130.0	57.7	0.827	36.9
	134.0	56.0	0.836	37.6

lookup tables for all systems, and Figure 109 shows the corresponding plots for maximum thrust conditions.

Analytical validation. We validated SSTSIM by comparing its results with 1) analytical approximations for motion along a straight and flat guideway, and 2) numerical results generated using the program MPS, previously used by the GMSA Team for system simulations.

The one-dimensional momentum and energy equations for motion along a straight, flat guideway are

$$T - R = ma \tag{17}$$

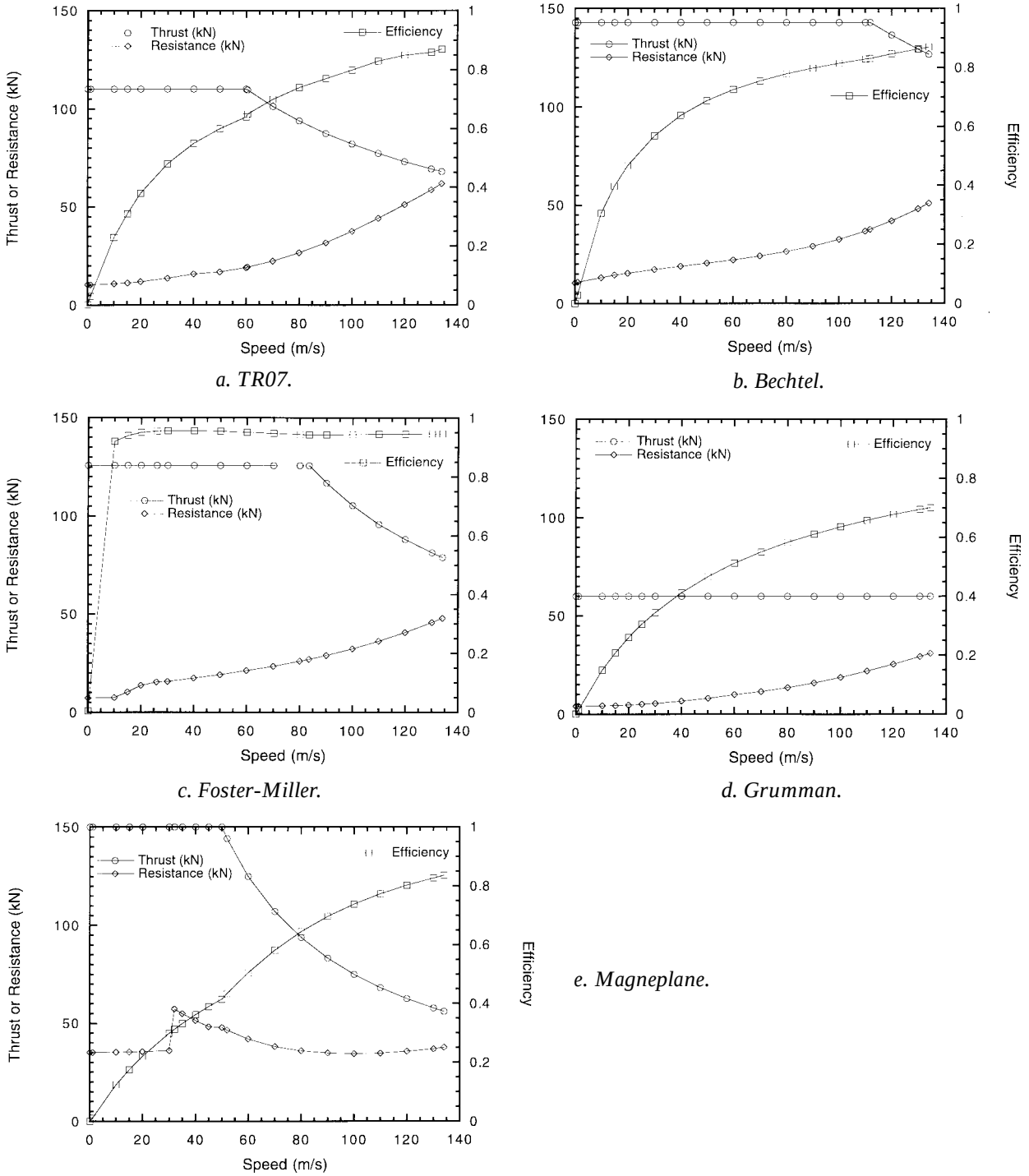

a. TR07.

b. Bechtel.

c. Foster-Miller.

d. Grumman.

e. Magneplane.

Figure 109. LSM and vehicle resistance vs. speed.

Table 42. Electrical energy (kWh) input to each LSM to accelerate the maglev vehicle from zero to 134 m/s. Normalization by the number of standard passengers (SP) corrects for differences in the space allocated per passenger in each vehicle.

E_{0-134}	*TR07*	*Bechtel*	*Foster-Miller*	*Grumman*	*Magneplane*
Equation 21	857	273	293	396	379
SSTSIM	852	278	293	397	382
E_{0-134} / SP	5.4	2.5	2.1	3.3	3.5

$$P = Tv \tag{18}$$

where T = LSM thrust
R = vehicle resistance
m = vehicle mass
a = vehicle acceleration
P = mechanical power provided by LSM
v = vehicle velocity.

Mechanical power provided by the LSM is related to the required electrical power P_e via the LSM efficiency η:

$$P = \eta P_e \ . \tag{19}$$

Combining these three equations and integrating yields the electrical energy required to move the vehicle:

$$E_{1-2} = \int_1^2 \frac{mv}{\eta}\, dv + \int_1^2 \frac{Rv}{\eta}\, dt \ . \tag{20}$$

The first integral is the electrical energy needed to accelerate the vehicle and the second is the electrical energy needed to overcome vehicle resistance (e.g., air and magnetic drag). If the vehicle is accelerating ($a > 0$), the second integral can also be expressed in terms of the change in velocity, $dv = adt$, to yield

$$E_{1-2} = m \int_{v_1}^{v_2} \frac{1}{\eta}\left[1 + \frac{1}{T/R - 1}\right] dv \ . \tag{21}$$

The two terms in the integral retain the same interpretations as in eq 20. For the maglev systems studied here, these terms are functions of velocity only. Note that the resistance contribution to E_{1-2} is small if thrust is much larger than resistance. That is, for a given change in velocity, the LSM will supply less energy to overcome vehicle resistance if the velocity changes quickly. The LSM efficiency as a function of velocity affects both terms in eq 21. To minimize trip time, acceleration occurs at maximum thrust, where efficiency is lowest. Thus, η has a strong influence on E_{1-2}.

Table 42 compares electrical energy required to accelerate each maglev vehicle from zero to 134 m/s calculated from eq 21 and obtained from SSTSIM (for the case of unconstrained acceleration). The deviations are small and attributable to numerical integration errors. Even allowing for differences in standard passengers (SP) carried, TR07 requires about twice the energy to accelerate to cruise speed as the SCD vehicles because its slow acceleration results in more time spent at inefficient, maximum thrust conditions.

We may calculate the trip time and energy consumption for a vehicle traveling along a straight and flat route if the speed profile is known. Figure 110 shows vehicle speed vs. time for straight and flat travel at the ride comfort limits. The Bechtel SCD can approximate this speed profile because it can accelerate at 0.16 g until it reaches about 120 m/s. Although its maximum acceleration drops to 0.12 g at 134 m/s, this adds only about 1 s to the time required to accelerate the vehicle to

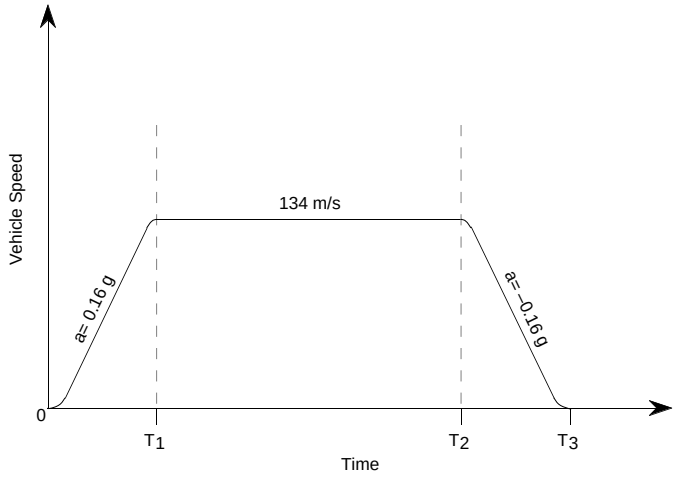

Figure 110. Vehicle speed profile along straight and flat route at ride comfort limits. Jerk limits require acceleration roll-on and roll-off at 0.07 g/s.

Table 43. Incremental time, distance, and energy required for the Bechtel vehicle to traverse a 40-km straight and flat route. Analytical results are for motion at the ride comfort limits.

	Time interval (s)		*Guideway length (m)*		*Energy used (kWh)*	
Phase	*Analytical*	*SSTSIM*	*Analytical*	*SSTSIM*	*Analytical*	*SSTSIM*
Acceleration	87.7	89.0	5,879	6,032	273	278*
Steady cruise	210.8	209.6	28,242	28,100	424	422
Braking	87.7	87.8	5,879	5,872	0	0
Total	386.2	386.4	40,000	40,004	697	700

* SSTSIM energy is for unconstrained acceleration, to compare with analytical value.

cruise speed. Table 43 compares analytical and SSTSIM results for the Bechtel vehicle to cover a 40-km straight and flat route. Allowing for the slightly longer time and distance required for the vehicle to accelerate to cruise speed, the results show excellent agreement. Because SSTSIM computes a braking path that just crosses each speed gate, the vehicle slightly overshoots the terminal stop. Use of a smaller time step reduces this overshoot.

We also compared SSTSIM and analytical results (braking paths, acceleration profiles, energy increments) for travel between nonzero speed gates, including the effects of grade changes. In all cases, SSTSIM results were in excellent agreement with analytical values.

Validation using Maglev Performance Simulator (MPS). The GMSA Team originally used a software package called Maglev Performance Simulator (MPS). Developed by J.E. Anderson Associates, MPS is a suite of eight programs that accepts as inputs the vehicle and LSM technical characteristics, the SST route alignment, and the ride comfort constraints. Like SSTSIM, it attempts to determine the acceleration and speed profiles that allow a vehicle to traverse the SST route in minimum trip time within these constraints. Unlike SSTSIM, however, MPS does not approximate the ride comfort requirements but rather designs each curve (three-dimensional entry and exit spirals) to ensure that the vehicle satisfies all ride comfort constraints.

The comprehensive MPS proved difficult to validate. In particular, the scheme to optimize curve designs did not always result in minimum trip time (e.g., very small increases in trip time could result when a secondary criterion such as lateral jerk was relaxed). That is, the vehicle always satisfied the ride comfort criteria through each curve but it didn't necessarily follow the bounding mathematical envelop defined by the ride comfort criteria. This is a minor shortcoming, and we may compare MPS results with those from SSTSIM to assess the validity of the latter, particularly the validity of approximating the ride comfort constraints.

SST simulations using the final version of MPS were completed only for TR07. The input LSM characteristics were slightly different from those shown in Table 41a, and the total tilt angle (i.e., guideway superelevation in TR07's case) was set at 11.2° rather than the actual value of 12°. Using these modified characteristics, we conducted SST simulations using SSTSIM and compared the results with those from MPS (see Table 44 and Figure 111). Deviations between the MPS and SSTSIM times and energies are typically within 0.5% everywhere along the SST route. Because MPS is entirely independent software, this confirms the validity of SSTSIM.

System comparisons using SSTSIM

We used SSTSIM to simulate the performance of TR07 and the four SCDs along the 40-km

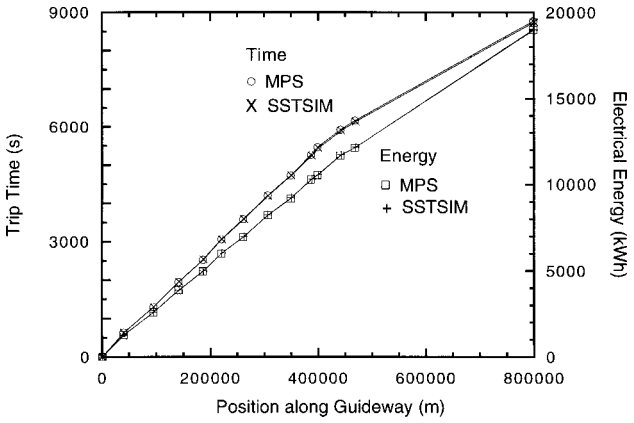

Figure 111. Comparison of SST results for TR07 simulated using SSTSIM and MPS with identical LSM and vehicle characteristics.